

PNNL-37190

# Experimental Investigation into Select Thermophysical Properties of the Potassium-Magnesium Chloride Salt System for Molten Salt Reactors

December 2024

Kyle Makovsky Michaella Harris Ji-Hye Seo Kent Detrick Jose Marcial Dallin Barton Jacqueline Royer



### **DISCLAIMER**

This report was prepared as an account of work sponsored by an agency of the United States Government. Neither the United States Government nor any agency thereof, nor Battelle Memorial Institute, nor any of their employees, makes any warranty, express or implied, or assumes any legal liability or responsibility for the accuracy, completeness, or usefulness of any information, apparatus, product, or process disclosed, or represents that its use would not infringe privately owned rights. Reference herein to any specific commercial product, process, or service by trade name, trademark, manufacturer, or otherwise does not necessarily constitute or imply its endorsement, recommendation, or favoring by the United States Government or any agency thereof, or Battelle Memorial Institute. The views and opinions of authors expressed herein do not necessarily state or reflect those of the United States Government or any agency thereof.

PACIFIC NORTHWEST NATIONAL LABORATORY

operated by

BATTELLE

for the

UNITED STATES DEPARTMENT OF ENERGY

under Contract DE-AC05-76RL01830

Printed in the United States of America

Available to DOE and DOE contractors from the Office of Scientific and Technical Information, P.O. Box 62, Oak Ridge, TN 37831-0062

www.osti.gov ph: (865) 576-8401 fox: (865) 576-5728 email: reports@osti.gov

Available to the public from the National Technical Information Service 5301 Shawnee Rd., Alexandria, VA 22312 ph: (800) 553-NTIS (6847) or (703) 605-6000

email: <a href="mailto:info@ntis.gov">info@ntis.gov</a>
Online ordering: <a href="mailto:http://www.ntis.gov">http://www.ntis.gov</a>

# Experimental Investigation into Select Thermophysical Properties of the Potassium-Magnesium Chloride Salt System for Molten Salt Reactors

December 2024

Kyle Makovsky Michaella Harris Ji-Hye Seo Kent Detrick Jose Marcial Dallin Barton Jacqueline Royer

Prepared for the U.S. Department of Energy under Contract DE-AC05-76RL01830

Pacific Northwest National Laboratory Richland, Washington 99354

# **Summary**

Considerable demand exists for fundamental research and development for molten salt reactors. Pacific Northwest National Laboratory (PNNL) contributes to this effort by providing fundamental thermophysical property measurements for molten salt systems. These data are ultimately bound for the Molten Salt Thermophysical Properties Database jointly stewarded by the University of South Carolina and Oak Ridge National Laboratory.

The work presented herein is aimed at providing select thermophysical properties of the potassium chloride-magnesium chloride molten salt system. The properties of specific enthalpy, heat capacity, density, and volatility were investigated in the temperature range of 500 to 800 degrees Celsius, at atmospheric pressure. Some of the techniques used to determine these properties are well-established at PNNL, while others are in-development. The work presented in this report are from techniques at all stages of development. As such, experimental theory, design, implementation, and results are presented for those still in development.

The effect of impurities on molten salt properties is generally under-explored in the research community. Thus, in addition to fundamental properties of pure salt mixtures, the effects of trace impurities are also explored. Namely, the effect of water on specific enthalpy and heat capacity. The effects of corrosion product surrogates such as iron, nickel, and chromium on specific enthalpy, heat capacity, and volatility.

Summary

# **Acknowledgments**

The authors would like to thank all the support staff at PNNL who make research at a National Laboratory possible. A special thank you to the wonderful administrators of the Nuclear Material Processing group.

Acknowledgments

# **Acronyms and Abbreviations**

°C Degrees Celsius µm Micrometer (micron)

μs Microsecond Å Angstrom

AIMD Ab initio Molecular Dynamics

BN Boron Nitride

BSE Backscattered Electron

CA Contact Angle

Cl Chlorine

CMD Classical Molecular Dynamics

cm<sup>3</sup> Cubic centimeter

Cr Chromium

CT-CPA Cold Trap-Condensed Phase Analysis

EDS Energy Dispersive Spectroscopy

EGA Evolved Gas Analysis

EGA-MS Evolved Gas Analysis-Mass Spectrometry

Fe Iron

FIB Focused Ion Beam
FY24 Fiscal Year 2024

g Gram

GPa Giga Pascals
H Hydrogen

hBN Hexagonal boron nitride

Hz Hertz

K Potassium

deg K Degrees Kelvin

KCl-MgCl<sub>2</sub> Potassium-magnesium chloride

KFT Karl Fischer Titration kJ mol<sup>-1</sup> Kilojoules per mole

kV Kilovolts

LIBS Laser Induced Breakdown Spectroscopy

MD Molecular Dynamics

Mg Magnesium
mg Milligrams
mJ Millijoules
mL Milliliters

mm Millimeters

mm<sup>2</sup> Square millimeters

mol% Mole percent
MPa Mega Pascals

MSR Molten Salt Reactor

N Newtons nA Nanoamps Ni Nickel

NIST National Institute of Standards and Technology

nm Nanometers
O Oxygen

PNNL Pacific Northwest National Laboratory

ppm Parts per million

ppmw Parts per million by weight rpm Revolutions per minute SE Secondary Electron

sec Seconds

SEM Scanning Electron Microscopy
TMA Thermomechanical analysis

wt Weight

wt % Weight percent XRD X-ray Diffraction

# **Contents**

Sumi	mary			ii
Ackn	owledg	ments		iii
Acro	nyms aı	nd Abbrev	viations	iv
1.0	Intro	duction		4
2.0	Expe	rimental A	Approach	5
	2.1	Sample	Preparation	5
	2.2	Materia	al Characterization	6
		2.2.1	Karl Fischer Titration	6
		2.2.2	Laser Induced Breakdown Spectroscopy	6
		2.2.3	Scanning Electron Microscopy and Energy Dispersive Spectroscopy	7
	2.3	Thermo	ophysical Property Analysis	7
		2.3.1	Enthalpy and Heat Capacity	7
		2.3.2	Density	8
		2.3.3	Volatility	9
3.0	Resu	ilts and D	iscussion	12
	3.1	Pre-An	alysis Material Characterization	12
	3.2	Thermo	ophysical Properties	16
		3.2.1	Enthalpy and Heat Capacity	16
		3.2.2	Density	21
		3.2.3	Volatility	23
4.0	Conc	lusion		48
5.0	Refe	rences		50
Appe	ndix A	<ul><li>Thermo</li></ul>	mechanical Analysis Sample Container Design	A.1
1.0	Back	ground		A.2
2.0	Theo	ry		A.4
3.0	Sam	ole Conta	iner Design	A.8
	3.1	Boundi	ng Conditions	A.8
		3.1.1	Temperature Limits	
		3.1.2	Chemical Compatibility	A.8
		3.1.3	Contact Angle	A.8
		3.1.4	Density Ratio	A.9
		3.1.5	Material Strength and Cost	
		3.1.6	Instrument Limits	
	3.2	Part De	esign	A.11
4.0	Conc	lusion		A.12

# **Figures**

Figure 1. Phase Diagram for the KCl-MgCl <sub>2</sub> salt system.	5
Figure 2. Schematic of the cold trap evolved gas analysis set up developed for this work.  Right-hand side shows cross-section of the inner part of the furnace where the sample is placed	11
Figure 3. Representative LIBS spectra for pure endmember salts used in this study	
Figure 4. Calibration curve used to verify the developed batching procedure and that representative subsamples are aliquoted from the bulk batch	
Figure 5. LIBS emission intensity versus shot for the 43 mol% KCl mixture. Black line shows Mg emission and gray line shows K emission. Note alternating and inverse relationship. This may account for the high apparent errors in the LIBS data.	15
Figure 6. Drop calorimetry derived specific enthalpy for the off the shelf salt series	
Figure 7. Drop calorimetry derived specific enthalpy for the ultra-dry salt series	
Figure 8. Drop calorimetry derived specific enthalpy for ultra-dry salts doped with 1 wt%	
water	18
Figure 9. Drop calorimetry derived specific enthalpy for ultra dry salts doped with 300 ppm by weight of Fe, Cr, and Ni	19
Figure 10. Drop calorimetry derived specific enthalpy for ultra dry salts doped with 600 ppm by weight of Fe, Cr, and Ni	20
Figure 11. Experimentally derived density curve for the 43 mol % KCl mixture between room temperature and 800 °C	22
Figure 12. Selected chlorine mass number release from 69 mol % KCl mixture; Left) same mixture ran in December. Samples derived from off-the-shelf salts. Right) 69 mol % ran in January taken from the ultra-dry batch prepared day of experiment in glovebox	
Figure 13. Hot stage XRD results of MgCl <sub>2</sub> at target temperatures	25
Figure 14. XRD spectra of 43 mol% KCl with peak identification.	
Figure 15. Vapor trail from MgCl <sub>2</sub> after completed scan (a) the back of the sample holder with subsamples collected from labeled sections (b) front of sample holder with a subsample taken from labeled section.	27
Figure 16. Photograph taken of the cold trap after the initial test run. The white substance is the condensed salt vapor. Length of cold trap tube visible in this photograph is approximately 200 mm	28
Figure 17. X-ray diffraction patterns for condensate and residue fractions from the 43 mol% KCl mixture.	29
Figure 18. X-ray diffraction patterns for condensate and residue fractions from the 65 mol% KCl mixture.	
Figure 19. X-ray diffraction patterns for condensate and residue fractions from the 69 mol% KCl mixture	
Figure 20. X-ray diffraction patterns for condensate and residue fractions from the 69 mol% KCl mixture doped with 300 ppm by weight Fe, Cr, and Ni	33

Introduction 2

Figure 21. Secondary electron images of the condensate and residue fractions for the 43 mol% KCl mixture. All figures containing SEM images are presented in a similar fashion, that is, two images from each condensate and residual fraction, at both a low magnification (1,000-2,000x; left) and high magnification (10,000-20,000x; right)	
Figure 22. X-ray emission maps derived from energy dispersive spectroscopy	
Figure 23. Secondary electron images of the condensate and reside fractions for the 65 mol% KCl mixture.	
Figure 24. X-ray emission maps derived from energy dispersive spectroscopy	38
Figure 25. Secondary electron images of the condensate and residue fractions for the 69 mol % KCl mixture.	
Figure 26. X-ray emission maps derived from energy dispersive spectroscopy	40
Figure 27. Secondary electron images of condensate and residue fractions for the 69 mol % KCl mixture doped with 300 ppm by weight Fe, Cr, and Ni	41
Figure 28. X-ray emission maps derived from energy dispersive spectroscopy	43
Figure 29. Calibration curve used to determine mol% KCl content for the condensate and residue fractions from LIBS spectral data	44
Figure 30. Plots of LIBS emission spectrum from 325 to 350 nm. Note small peak at 341.5 nm, resulting from the presence of Ni in the condensate fraction.  Nickel was the only doped impurity identified in the condensate fraction	47
Figure 31. Two cross-sections of a typical TMA crucible (white) containing salt (blue) at two different times. a.) Just after melt. b.) Sometime between melt and the end of the measurement, salt leaks from the annular region between the plunger and the crucible wall.	A.3
Figure 32. Pressure diagram for the TM sample container system	A.5
Figure 33. Cross-section of hollow plunger used to reduce density ratio.	A.9
Tables	
Table 1. Results of moisture analysis via Karl Fischer Titration	12
Table 2. Tabulated results of specific enthalpy data determined by drop calorimetry.  Mean values have units of kilojoules per mole (kJ/mol). n.d not determined	20
Table 3. Comparison of densities derived by experimental (this work) and molecular dynamic modeling. Values in this table have units of grams per cubic centimeter (g/cm3). *Density values from personal communication with Manh Nguyen, 2024	
Table 4. Phases and their percentage compositions in residue and condensate fractions for select runs determined by XRD analysis.	34
Table 5. Results of LIBS spectral analysis for condensate and residue fractions for all eutectic compositions tested	45
Table 6. Maximum wt% concentrations of impurities in high-purity hBN grades	
Table 7. Material strength properties of high purity hBN grades.	A.11

Introduction 3

# 1.0 Introduction

Thermophysical properties are rated as the highest priority focus area for research and development based on the functional needs of molten salt reactor (MSR) design (Betzler et al., 2019). The thermal hydraulic design of the MSR relies on properties such as density, specific heat capacity, and vapor pressure and volatility (Noorie-Kalkhoran et al., 2022). The behavior of the molten salt during operation is dependent on the thermodynamic properties of the components, many of which are covariant, and each serves an individual purpose to the importance of reactor operation.

Impurities in molten salt have a largely unknown effect on their thermophysical properties. Impurities may be derived from processes related to manufacture, environmental contamination, or from corrosion and subsequent leaching of containment material components. For example, recent work by Hartmann and Paviet (2022) provided a review on the mechanisms responsible for corrosion of molten salt reactor containment materials. Work in Fiscal Year 2024 (FY24) focused on addressing the lack of information related to impurities and their effect on thermophysical properties relevant to molten salt reactor design and operation.

The binary potassium-magnesium (KCl-MgCl<sub>2</sub>) system has been considered as a coolant in molten salt reactors (Anderson and Sabharwall, 2012). Additionally, it has been used in solar energy applications (Xu et al., 2018; Li et al., 2020). This system has many attractive properties. As a heat transfer and thermal storage material, it can operate at temperatures as high as ~1400 degrees Celsius (°C), indicating its high thermal stability (Xu et al., 2018). Moreover, it has a low viscosity and vapor pressure (Li et al., 2017; Xu et al., 2018). Both Mg and K are found in easily exploitable natural resources, such as seawater (Culkin and Cox, 1966; Abdel-Aal, 2018). This makes their extraction relatively inexpensive and is one reason why this system has gained considerable attention in both solar power thermal storage and molten salt reactor applications.

The main goals of this work are twofold: 1) to experimentally derive specific enthalpy and heat capacity, density, and volatility of pure  $KCl-MgCl_2$ ; and 2) to introduce trace impurities in known amounts to these pure salts, measure the same thermophysical properties, and evaluate the impact of these impurities on the measured properties. To accomplish these goals, a variety of analytical methods were used, each of which are described in detail in the experimental section of this report.

Introduction 4

# 2.0 Experimental Approach

# 2.1 Sample Preparation

A phase diagram for the KCl-MgCl<sub>2</sub> system is shown in Figure 1 (Perry and Fletcher, 1992). This system contains three eutectic points with compositions of 69, 65, and 43 mol% KCl. These three compositions along with the pure endmember phases were chosen for experimental analysis. Importantly, molecular dynamic (MD) modeling by previous studies (e.g., Lu et al., 2021) and ongoing modeling efforts at Pacific Northwest National Laboratory (PNNL) of these compositions provide a benchmark to which this experimental work may be validated. Additionally, samples of the same eutectic compositions were doped with 300 and 600 parts per million by weight (ppmw; total impurities, ) of iron (Fe), nickel (Ni), and chromium (Cr) chlorides as a surrogate test for the incorporation of corrosion products from a stainless steel containment vessel. Lastly, the eutectic compositions were doped with 1 weight percent (wt%) water (H<sub>2</sub>O) to simulate the adsorption of environmental moisture (Table 1). Details of the batching method may be found in previous iterations of this work (e.g., PNNL-35354).

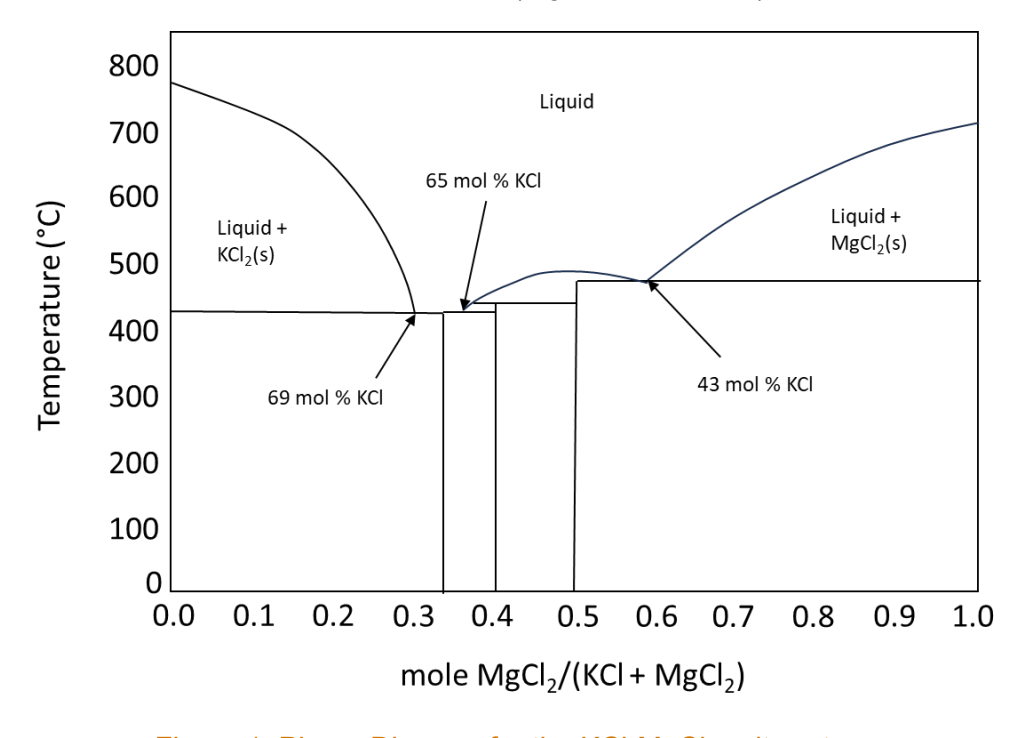


Figure 1. Phase Diagram for the KCl-MgCl<sub>2</sub> salt system.

Pure MgCl<sub>2</sub> and KCl salts of two pedigrees were used for this work. Initially, the inventory available contained these two salts (KCl and MgCl<sub>2</sub>; American Elements, 99.99% metals basis, Los Angeles, CA) but they had been stored on the shelf in air for an unknown period of time. Given the hygroscopic nature of both of these salts, especially MgCl<sub>2</sub>, it was deemed necessary to determine potential incorporation of environmental contaminants (e.g., H<sub>2</sub>O) prior to their use in testing. To test this, Karl Fischer Titration (KFT) was used. Details of the KFT analyses are in section 2.2.1

In addition to the concern of water, it was unknown whether the previous batching method was amenable to aliquoting representative subsamples. To assess this, after each pellet was

analyzed by KFT, the pellets were analyzed for their bulk chemistry to verify molar ratios. Details of this analysis are in section 2.2.2.

Sample preparation of the second pedigree of salts varies from the aforementioned salts in many ways and is believed to be a significant improvement over the previous sample preparation methodology. Potassium chloride (Fisher Scientific, ultra dry 10 mesh beads, 99.95% metals basis, Waltham, MA) and magnesium chloride (Alfa Aesar, ultra dry powder, 99.9% metals basis. Haverhill, MA) were purchased from Fisher Scientific. These salts are manufactured, stored, and stored under argon, and were opened in a positive-pressure inert (nitrogen atmosphere) glovebox at PNNL. Within the same glovebox, 50 grams (g) of each composition were batched and manually ground using a diamonite mortar and pestle. The ground powder was further processed using a micro vibration mill (MTI Corp., model MSK-SFM-12M-A-LD, Richmond, CA, USA) in 5 g batches using 2 milliliter (mL) polypropylene tubes. Each 5 g batch was milled with a vibrational speed of 4000 revolutions per minute (rpm) for two hours. After each 5 g batch had been processed, the total 50 g batch was recombined. It was from this container that subsamples were taken for subsequent analyses. Similar to above, to assess the efficacy of the new batching process, three 20 mg subsamples were aliquoted from each batched and ball milled sample. Each 20 mg sample was pelletized using a manual mechanical press (MTI Corp., model EQ-YLJ-3, Richmond, CA, USA) and a 6-millimeter (mm) diameter pellet die. The pellets were then analyzed for their bulk chemistry to verify acceptable molar ratios. Details of this analysis are in section 2.2.2.

### 2.2 Material Characterization

### 2.2.1 Karl Fischer Titration

Coulometric Karl Fischer Titration is a high sensitivity technique for tracing water content (i.e., 0.001 to 1%). A detailed discussion of the fundamentals in KFT is beyond the scope of this work, but a general discussion of its operating principles is outlined herein.

Water content is determined by measuring the voltage drop created by the conversion of iodide  $(I^{-})$  to iodine  $(I_{2})$ . This conversion is supported via the oxidation of sulfur dioxide  $(SO_{2})$ :

$$I_2 + SO_2 + H_2O \rightarrow 2HI + SO_3$$

Eqn. 1

100 milligrams (mg) of sample powder were pelletized using either a Carver 4350 Manual Hydraulic Press (Carver, INC., Wabash, IN, USA) with a 12 mm diameter die or the EQ-YLJ-3 mechanical press (described above) for off-the-shelf and ultra-dry salts, respectively. Each composition was pressed in triplicate. The pelletized sample was introduced into the tube furnace (Kyoto Electronics Manufacturing Co., Model ADP-512, Kyoto, Japan) via a sliding glass tray. A constant supply of nitrogen was purged through the furnace where it captured moisture liberated from the sample and transferred it into the KFT cell (Kyoto Electronics Manufacturing Co., Model MKC-710S, Kyoto, Japan). Nitrogen was bubbled through the anolyte where the water previously contained in the sample was then consumed in the KFT reaction. The furnace was set to 120 °C and each measurement was taken over a duration of 15 minutes.

# 2.2.2 Laser Induced Breakdown Spectroscopy

Laser Induced Breakdown Spectroscopy (LIBS) is an *in situ* sampling technique whereby a high-powered, pulsed laser is directed at a sample surface. As the incident laser interacts with the surface, a very small amount of material is ablated, and a short-lived plasma is produced.

The highly energetic nature of the plasma liberates electrons from atoms contained within it. Upon de-excitation, light is emitted at wavelengths characteristic to the elements present in the plasma (and thus, the sample). A spectrograph is aimed at the plasma to collect this light and is displayed on a computer.

Analyses were conducted using an Applied Spectra, Inc. J200 LIBS-only system (Applied Spectra, Sacramento, CA). Typical conditions for analysis are as follows: laser energy 1-5 millijoules (mJ), laser repetition rate 10 hertz (Hz), spot size 35 microns ( $\mu$ m), gate delay 0.5 microseconds ( $\mu$ s), and gas flow rate of 500 mL/minute. All samples were analyzed in an inert atmosphere containing helium (He). Helium was preferred for these analyses to both improve sample to noise ratio and to suppress a strong K peak at 766.49 nanometers (nm) caused by the high K content of the samples.

LIBS was used for verification of batched molar ratios and for characterization of condensed solids for the volatility experiments (outlined below). Spot analysis differed between the two sample types. For those pelletized, each pellet was analyzed using a 5x5 grid of points with physical dimensions approximately 100 mm². At each location, 25 spectra were collected. Thus, 625 spectra were collected for each pellet. A single emission line was used for K, Mg, and Cl at 766.49 nm, 383.83 nm, and 837.62nm, respectively. Peak height values at each location were averaged over the entire 625 spectra collected and the K/Cl ratio determined. For condensate samples, salt was collected and placed onto a 25.4 mm aluminum pin stub mount containing 2-sided carbon tape, typically used in scanning electron microscopy (SEM). Twenty-five analytical spots were randomly chosen with one shot taken at each location. The average peak height values for K and Mg were determined and the K/Mg ratio calculated.

# 2.2.3 Scanning Electron Microscopy and Energy Dispersive Spectroscopy

Additional material characterization was performed using scanning electron microscopy (SEM) and energy dispersive spectroscopy (EDS). This technique was only used for products of the volatility experiments. Secondary electron (SE) and backscattered electron (BSE) images were collected using a Helios 5 UX focused ion beam (FIB) SEM (ThermoFisher, Waltham, MA), with typical beam conditions of 15 kilovolts (kV) accelerating voltage and 0.11 nanoamps (nA) beam current. Elemental data were collected using an Ultim Max 170 mm² silicon drift detector (Oxford Instruments, Abingdon, UK). The same beam conditions were used for energy-dispersive spectroscopy (EDS) data collection as that used for imaging.

# 2.3 Thermophysical Property Analysis

# 2.3.1 Enthalpy and Heat Capacity

Enthalpy was measured using a high temperature drop calorimeter (Calvet DC Alexsys, Setaram, KEP Technologies, France) The drop calorimeter can indirectly measure standard enthalpy by using a correction factor derived from Shomate's equation for enthalpy (Eqn. 2; NIST WebBook).

$$H^{\circ} - H^{\circ}_{298.15} = A * t + B * t^{2}/2 + C * t^{3}/3D * t^{4}/4 - E/t + F - H$$
 Eqn. 2

where H° is the standard enthalpy of the solid or liquid state depending on the temperature (kilojoules per mole, kJ mol⁻¹), H°298.15 is the enthalpy under standard state conditions (kJ/mol), A-H are standard values listed for the specific compound from National Institute of Standards and Technology (NIST) given a range of temperatures (Kelvin, K), and t is the

temperature of the sample divided by 1000 (K). The alphabetical numbers are standardized and can be found in the NIST Chemistry WebBook.

Custom designed and fabricated nickel crucibles were used to withstand the corrosivity of the salts during a heating profile. Approximately 20 milligrams (mg) of salt were weighed in an inert glovebox. Using a benchtop iWeld laser welder (LaserStar Technologies, Orlando, FL), crucible lids were welded to seal the contents and reduce the release volatile salt during the experiment.

The following procedure was used for analysis via high temperature drop calorimetry. The three temperature control zones of the instrument were held at an isotherm at target temperatures (400-800°C). The instrument was allowed to equilibrate for 24-48 hours. After equilibrium was achieved, a background measurement was performed for eight hours to establish the instrument noise. The background measurements determined when subsequent samples would be dropped. A baseline measurement was taken in triplicate with empty nickel crucibles then samples were dropped in triplicate. The Callisto Processing (Setaram, KEP Technologies, France) software's peak integration function was used to determine the total signal from individual drops. Specific enthalpy was determined when the signal was tabulated. Specific enthalpy plotted against temperature (K) produced a slope defined as heat capacity for the salt.

# 2.3.2 Density

Density was measured using a form of dilatometry. This is a new approach at PNNL to measure density and as such, significant effort was placed on method development. Here, a thermomechanical analyzer (TMA; Netzsch 402 Hyperion F1, Selb, Germany) was utilized with a series of custom fabricated crucibles of two material types. This instrument is capable of accurate and precise measurements of very small changes in length, with an advertised digital resolution of 0.125 nanometers (nm); therefore, it is well-suited to measure changes in density associated with phase changes on minute amounts of material (< 20 mg). Although work in FY24 focused on non-radiological salts, future work with actinide-bearing salts is anticipated. Hence, it is advantageous to develop a method in which only small amounts of material are required for analysis.

For a given container volume, the fraction of that volume occupied by a material will change upon phase transition, e.g., from a solid to a liquid. This may be measured by a dilatometer if the material is only allowed to change in one dimension. As such a two-piece sample crucible was designed whereby only the height changes upon expansion during phase change from solid to liquid. Two crucible designs were tested, one made of pure nickel and the other made of alumina. Nickel rod-stock with a 12 mm diameter was previously purchased and cut into sections 25 mm long. A blind hole 10 mm in diameter is then machined into the rod to a depth of 20 mm. This serves as the crucible base. From a different piece of cut rod stock, the rod is machined to an outer diameter of 9.80 mm and serves as the plunger. This leaves nominally 0.20 mm clearance between the outer diameter of the plunger and the inner diameter of the crucible to allow for thermal expansion. The second crucible design tested is made of alumina, which was chosen due to its relatively minimal volumetric thermal expansion compared to nickel in the temperature range of interest. The alumina crucibles were fabricated in a similar manner. However, given no prior experience with alumina for this technique, it was necessary to determine the required clearance between the inner diameter of the crucible base and the outer diameter of the plunger. To do this, two plungers were fabricated with outer diameters of 7.880 and 7.900 mm. The crucible base was machined to an inner diameter of 8.000 mm, leaving 0.120- and 0.100- mm clearance, respectively.

The measurement principle behind TMA uses the volume change associated with the phase transition between solid and liquid. This volume change is translated to a change in the height of the plunger in the crucible, which results in a change in the height of the pushrod in the TMA. The height of the sample crucible is expressed in the unitless value of  $dL/L_o$ , where dL is the change in length,  $L_o$  is the starting length. Thus, a positive  $dL/L_o$  value represents a net lengthening whereas a negative  $dL/L_o$  value represents a net shortening. A graphical representation of this is made by plotting  $dL/L_o$  versus temperature. For this technique to work, the density of the sample must be determined a priori. Density values of the starting mixture were calculated using a simple mass balance approach, e.g., a 50/50 mixture of two materials with densities of 1 and 2 grams per cubic centimeters (g/cm³) would have a bulk density of 1.5 g/cm³. This information along with the dimensions of the crucible are entered into the software. Based on these inputs and from the change in length of the crucible measured during the experiment, the software calculates density using the following equation:

$$\rho(T) = \rho(r)T(r) \frac{\left(1 + \frac{\Delta L(T_r)}{L_0}\right) \cdot \left(1 + \alpha_C(T_r)\right)^2}{\left(1 + \frac{\Delta L(T)}{L_0}\right) \cdot \left(1 + \alpha_C(T)\right)^2}$$
 Eqn. 3

Where  $\rho(r)$  is the reference density,  $T_r$  is the reference temperature,  $\frac{\Delta L(T_r)}{L_0}$  is the initial displacement at  $T_r$ ,  $\frac{\Delta L(T)}{L_0}$  is displacement measured at experiment temperature, and  $\alpha_C$  is the linear thermal expansion coefficient for the crucible material.

Measurements via TMA were conducted across a standard set of conditions. Approximately 20 mg of batched material was pelletized using the mechanical pellet press using an 8mm pellet die. Pellets were loaded into the crucibles in the glovebox and transferred to the TMA. Analysis was conducted over the temperature range of 500-800 °C using a ramp rate of 10 °C/min. A minimal force of 0.001 Newtons (N) was applied to the pushrod, the minimum force achievable by the instrument. The furnace atmosphere was purged with ultra-high purity argon at a flow rate of 20 mL/min.

### 2.3.3 Volatility

### 2.3.3.1 Evolved Gas Analysis- Mass Spectrometry

Several methods were deployed to determine the volatile nature of the salts, the first preliminary tests were conducted using an evolved gas analysis (EGA) mass spectrometer (HPR-20 R&D EGA, Hiden Analytical Ltd. Warrington, U.K.). The instrument configuration consisted of a furnace with a quartz tube sample holder, carrier gas lines, and a heated capillary line connecting the flow of sample gas to the EGA. A standard set of experimental parameters were used in EGA experiments. The tare mass of the high purity quartz tube (30 x 2.5 cm) was taken, followed by adding approximately two grams of sample to the tube, then the final mass measured. The tube was placed in the furnace and flushed with an overflow (50 mL/min) of argon or nitrogen depending on the experiment. Once the gas reading stabilized in the output of the instrument the sample was ramped at a rate of 10 °C/min to the target temperature of 500, 600, 700, and 800 °C, where an isothermal hold of ten minutes occurred.

# 2.3.3.2 X-ray Diffraction

To determine if chemical reactions or phase changes had occurred after EGA measurements or during the melt of a salt, x-ray diffraction (XRD) was used. Powder XRD was executed using a Bruker D8 X-ray Diffractometer (XRD) (Bruker, Billerica, MA), and proprietary onboard software was used for data acquisition. The instrument is equipped with a high efficiency turbo x-ray source (TXS-HE) (Bruker, Billerica, MA), and a copper K- $\alpha$ 1 anode that has an x-ray wavelength of 1.541 Å (Angstrom; 0.1541 nm). Samples were prepared and level-packed in 25 mm diameter polymethyl methacrylate sample holders. Spectra were collected at a step rate of 0.015° 20/scan over the range of 10-60° 20.

A non-ambient sample changer referred to as a hot stage, equipped with the D8 XRD, was used to analyze sample temperatures below and above the melting point of the KCl-MgCl<sub>2</sub> series. A platinum heat strip is attached to thermocouples to supply conductive heat to the sample. A 100 mg manually pressed pellet was used for testing. The preparation and pressing of the pellet took place in an inert atmosphere glovebox and were transferred in a sealed container to reduce ambient atmosphere exposure. The measurements were taken in a helium environment. An initial measurement was taken at room temperature to align the system and verify the peak position. The first scan was taken at 30 °C. After the starting scan the stage was heated at a rate of 10 °C/sec, depending on the salt, to 25 °C below the melting point of the sample. Once a spectrum was collected below the melting point, another scan was taken at 25 °C above the melting point of the sample. Finally, at a cooling rate of 10 °C/min the last spectrum was taken at 30 °C. Each scan occurred after a 440-second dwell, at a rate of 0.2 sec/step.

# 2.3.3.3 Cold Trap Condensed Phase Analysis

A novel approach to measuring volatility was spurred by the discovery of a condensed vapor trail observed in the hot stage XRD experiments. This newly developed technique is simple and effective albeit with less temporal or thermal resolution as an ideal thermogravimetric (TGA)-EGA measurement. To the author's knowledge this is the first application of this technique aimed at understanding the volatile nature of chloride molten salts, which we are here coining Cold Trap Condensed Phase Analysis (CT-CPA).

The CT-CPA method uses a standard tube furnace into which a temperature-controlled cold trap is inserted (Fig. 2). The tube furnace utilized contains alumina tubes with an inner diameter of 42 mm (MTI GSL-1500X, Richmond, CA). A flange is connected to both sides of the furnace tube and each has gas port needle valves along their axes. The cold trap tube consists of a 9.525 mm (3/8 inch) diameter 316 stainless steel tube. After the flanges are connected to the furnace tube, the cold trap tube is then inserted completely through the furnace. At both ends of the cold trap tube, 9.525 mm compression fittings are connected to it; the compression fittings are secured to the flanges via a standard vacuum style fitting (KF25). Supply and return lines made of rubber tubing are then connected to either end of the cold trap tube. These lines are connected to a water-filled chiller. Finally, the gas lines are secured. Once the sample is loaded the furnace is purged with ultra-high purity nitrogen at a rate of 40-50 mL/min for the duration of the experiment. Approximately 200 mg of the sample is placed onto a high-purity platinum foil and loaded into the furnace. In this configuration, the cold trap tube is approximately 10 mm above the solid sample. As the sample is heated it begins to volatilize. The rising vapors meet the cold trap and due to the large temperature differential, they condense onto it. All samples were brought to 850 °C and held at this temperature for 120 minutes. After each experiment, the condensed solids on the cold trap (condensate) were sampled as well as the remaining material

on the platinum foil (residue). The condensate and residue fractions were characterized by XRD, LIBS, and SEM-EDS.

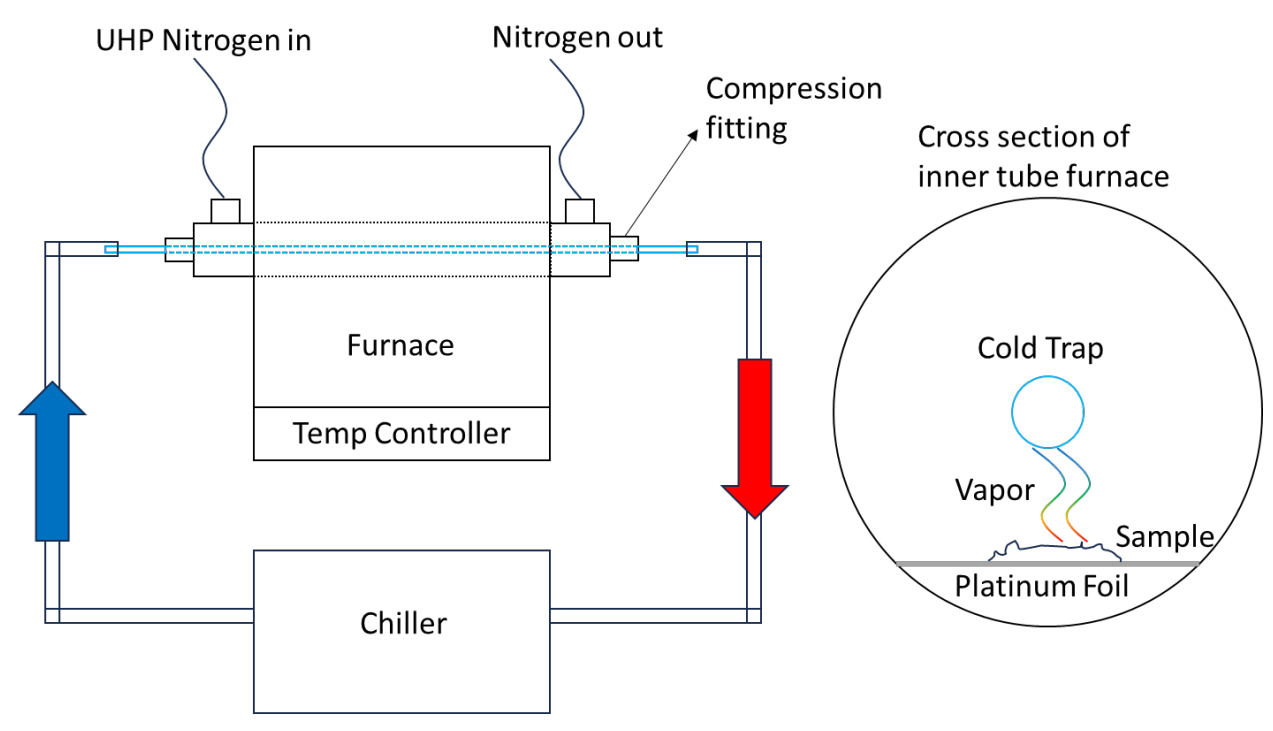


Figure 2. Schematic of the cold trap evolved gas analysis set up developed for this work. Right-hand side shows cross-section of the inner part of the furnace where the sample is placed.

# 3.0 Results and Discussion

# 3.1 Pre-Analysis Material Characterization

Replicate analysis via KFT reveal a marked difference between samples that were stored in atmosphere versus those that were manufactured, sealed, and opened in an inert environment. Table 1 highlights the differences observed, where the ultra-dry salts appear to contain 1-2 orders of magnitude less water. This highlights the necessity to store and handle KCl and MgCl<sub>2</sub> (and likely other chlorides as well) in a controlled atmosphere. Furthermore, should the off-the-shelf salts have been used for downstream thermophysical property testing, it is likely their 0.1-1.0+ wt% water content would have negatively impacted those results. For example, it is well-known as little as 1-2 wt% water can have significant impacts on the melting temperature (for a given pressure) of silicate materials (e.g., Johannes and Holtz, 1996). It therefore stands to reason a similar trend could be observed in chloride salts. Based on these results, only ultra dry compositions were used for thermophysical property testing, including salts that were batched for both impurity and water content. The single exception is for the 1 wt% water content samples analyzed for specific enthalpy and heat capacity via drop calorimetry, as most of the off-the-shelf salts exhibited water contents near 1%.

Water content in the ultra-dry salts is not zero. Despite best handling practices it is possible some of the measured water was incorporated into the material (e.g., absorption, adsorption, etc.) while in transport from the glovebox to the Karl Fisher instrument or from the glovebox itself as the water content typically ranged from 1-2 ppm. However, this transit time is only 5-10 minutes in a climate where low relative humidity prevails. It is not likely the measured water can be explained by this. Instead, water contamination is likely due to multiple sources culminating between the time of manufacture and the time of testing.

Table 1. Results of moisture analysis via Karl Fischer Titration.

Eutectic	Sample ID	Mass (mg)	Temp (deg C)	Mass H2O (ug)	Concentration (ppm)	ppm/mass pellet	Avg	Sd	RSD
4357_1	09-84	183.9	115	2461.6	13386	72.8			
4357_2	09-85	129.4	111	1602	12380	95.7			
4357_3	09-86	229.5	117	1916.3	8350	36.4	68.3	29.9	43.8
6535 1	09-87	101.5	107	506.6	4991	49.2			
6535 2	09-88	204.9	112	575.4	2808	13.7			
6535 3	09-89	220.3	110	759.8	3449	15.7	26.2	19.9	76.2
6931 1	09-90	128.5	110	1028.4	8003	62.3			
6931_2	09-91	186.4	110	1278.4	6858	36.8			

6931_3	09-92	192.1	110	1373.7	7151	37.2	45.4	14.6	32.1
4357_1	09-93	160.7	110	22.1	138	0.9			
4357_2	09-94	100.8	110	4.5	45	0.4			
4357_3	09-95	100.2	110	85.4	852	8.5	3.3	4.5	138.9
6535_1	09-96	164.9	110	10.8	65	0.4			
6535_2	09-97	127.2	110	57.4	451	3.5			
6535_3	09-98	212.3	110	76.5	360	1.7	1.9	1.6	84.2
6931_1	09-99	180.9	110	69.4	384	2.1			
6931_2	09-0900	80.7	110	78.6	974	12.1			
6931_3	09-0901	156.6	110	78.2	499	3.2	5.8	5.5	94.3

Relative molar proportions of most mixtures play a significant role in their properties. The goal of this work is to provide high-fidelity data for specific molar concentrations (i.e., eutectic compositions) within the KCI-MgCl<sub>2</sub> salt system. It is therefore paramount the salt compositions are verified prior to thermophysical property testing. To do this, pelletized salts were analyzed via LIBS.

Pure endmember and eutectic compositions were pelletized, and their LIBS spectroscopic properties were evaluated. Broadband spectroscopy (~190-1080 nm) reveals a relatively simple emission profile for K, Mg, and Cl (Fig. 3). Minimal trace metal impurities were identified with the exception of Ca in several spectra within MgCl<sub>2</sub> and Na in KCl. Oxygen was identified in both salts and H was identified in MgCl<sub>2</sub>. Although LIBS is typically not sensitive to molecular species (at least with the analytical conditions used), it is possible based on the presence of these elements that either water or magnesium oxide (MgO) is present in the sample.

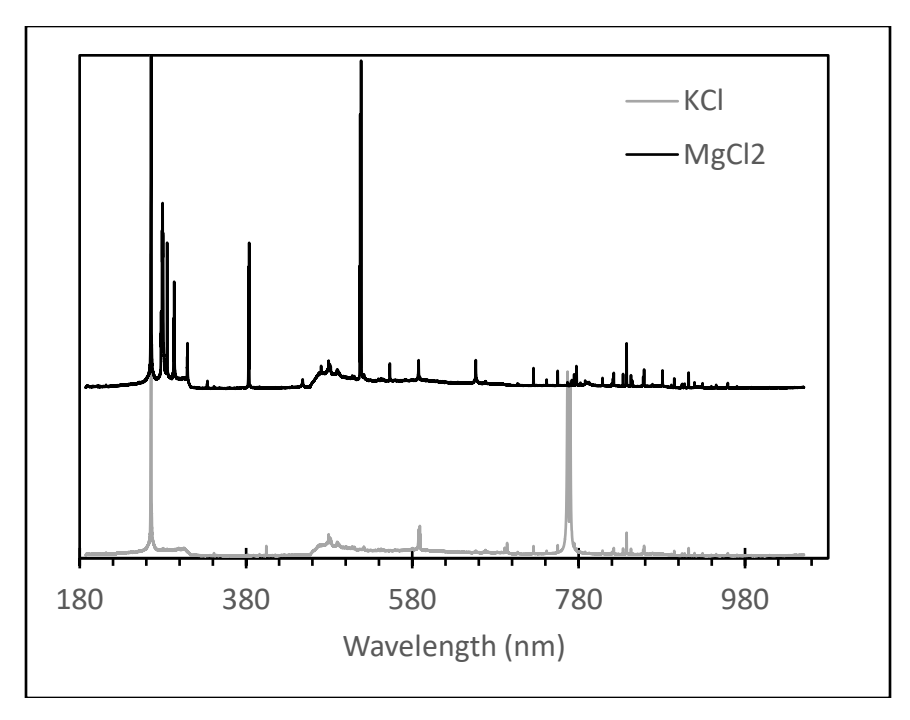


Figure 3. Representative LIBS spectra for pure endmember salts used in this study.

A calibration curve was developed from the spectral data to assess batched molar compositions. Average K and Cl peak height values were calculated, and K was normalized to CI. Normalization is a common data analysis technique used in LIBS because of the heterogeneity often observed in individual peak heights. Figure 4 shows the resulting calibration curve. The results show excellent linearity with a Pearson's correlation coefficient value (R2) of 0.98. Based on residuals calculated from this calibration curve, batched ratios are within 5% of the anticipated ratio. It should be noted the apparent error in the LIBS measurement is high. Figure 5 is an example from the 43 mol% KCl sample and provides a possible explanation for the apparent high error. As mentioned above, 25 shots were collected at each location. From one location to the next, there appears to be an inverse relationship between K and Mq intensity (Fig. 5). The sample preparation process involved vibration milling the batched salts, which produces a very fine powder product (as of yet particle size not determined). However, it seems the generated particle size from milling is still large enough that an individual location sampled by the laser (spot size 35 µm) can still be dominated by the presence of a KCl or MgCl<sub>2</sub> particle. This is likely the cause of the high apparent error. However, the K/Cl ratio determined by averaging all locations (within a given sample) produces a calibration curve with a high correlation to the expected bulk mol% KCl composition. Thus, confidence is high that the batching and subsampling method described above is conducive to the ultimate goal of producing high-fidelity thermophysical property data.

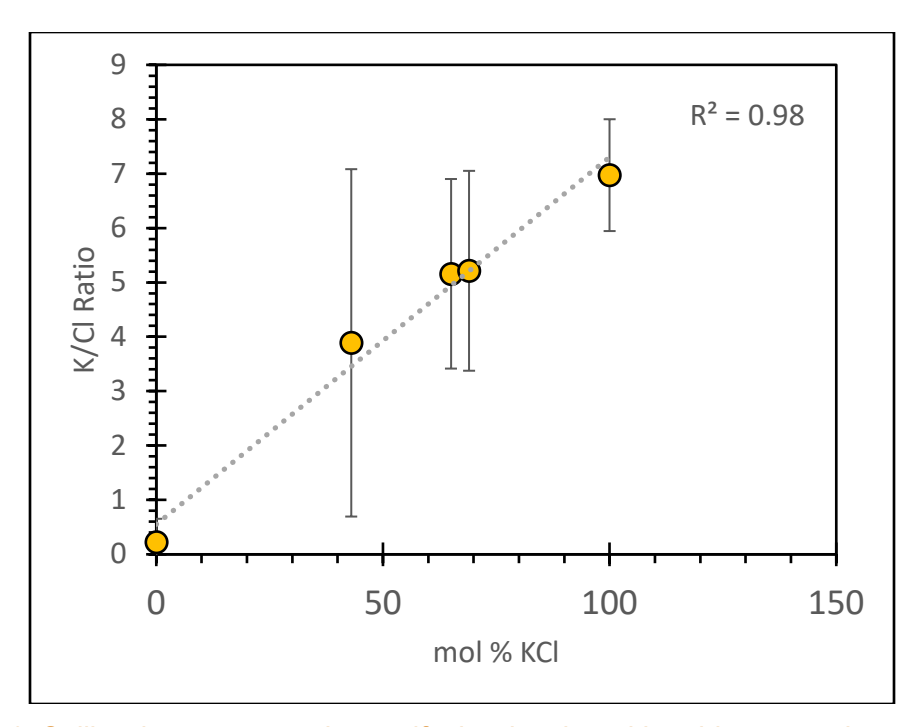


Figure 4. Calibration curve used to verify the developed batching procedure and that representative subsamples are aliquoted from the bulk batch.

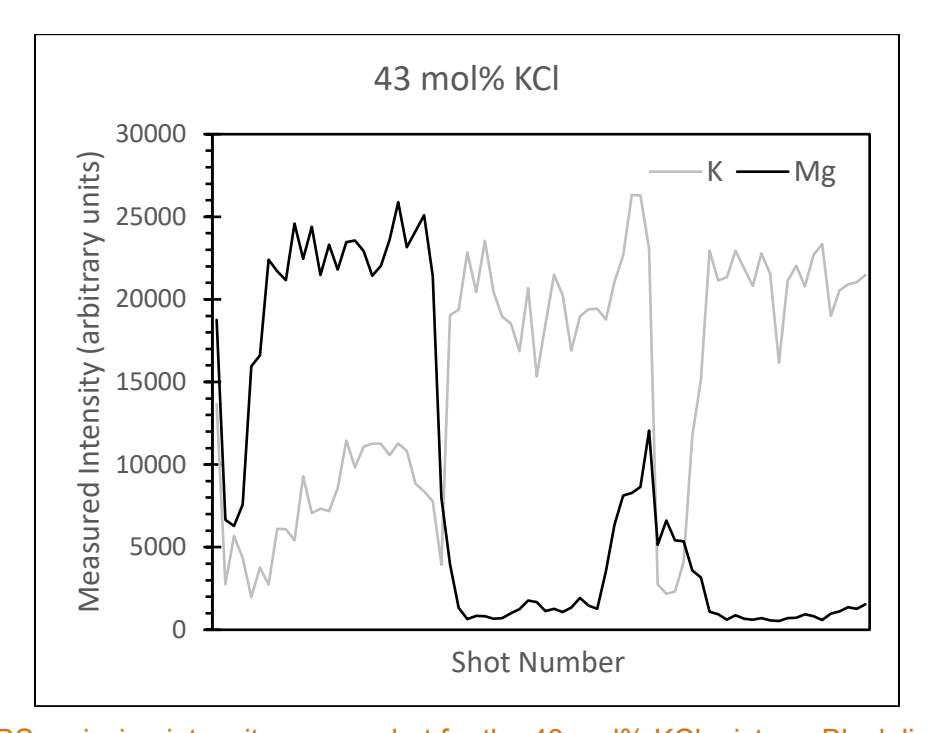


Figure 5. LIBS emission intensity versus shot for the 43 mol% KCl mixture. Black line shows Mg emission and gray line shows K emission. Note alternating and inverse relationship.

This may account for the high apparent errors in the LIBS data.

# 3.2 Thermophysical Properties

# 3.2.1 Enthalpy and Heat Capacity

Heat capacity values produced from the slope of enthalpy were compared to the simulated and experimental values presented in Lu et al. (2021) to verify the method and calculations for this specific system.

Specific enthalpy data were collected using the high temperature drop calorimeter on four salts systems, the off-the-shelf salts, the ultra-dry salts, salts containing 1 wt% water, and trace impurity containing salts with 300 ppm and 600 ppm levels of contaminates. A two-sample t-test between the ultra-dry and off-the-shelf salts was performed. P-values ranged between 0.1-0.4 depending on the composition being tested. Both KCl and MgCl<sub>2</sub> are within 10% error of the literature values (Figures 6 and 7).

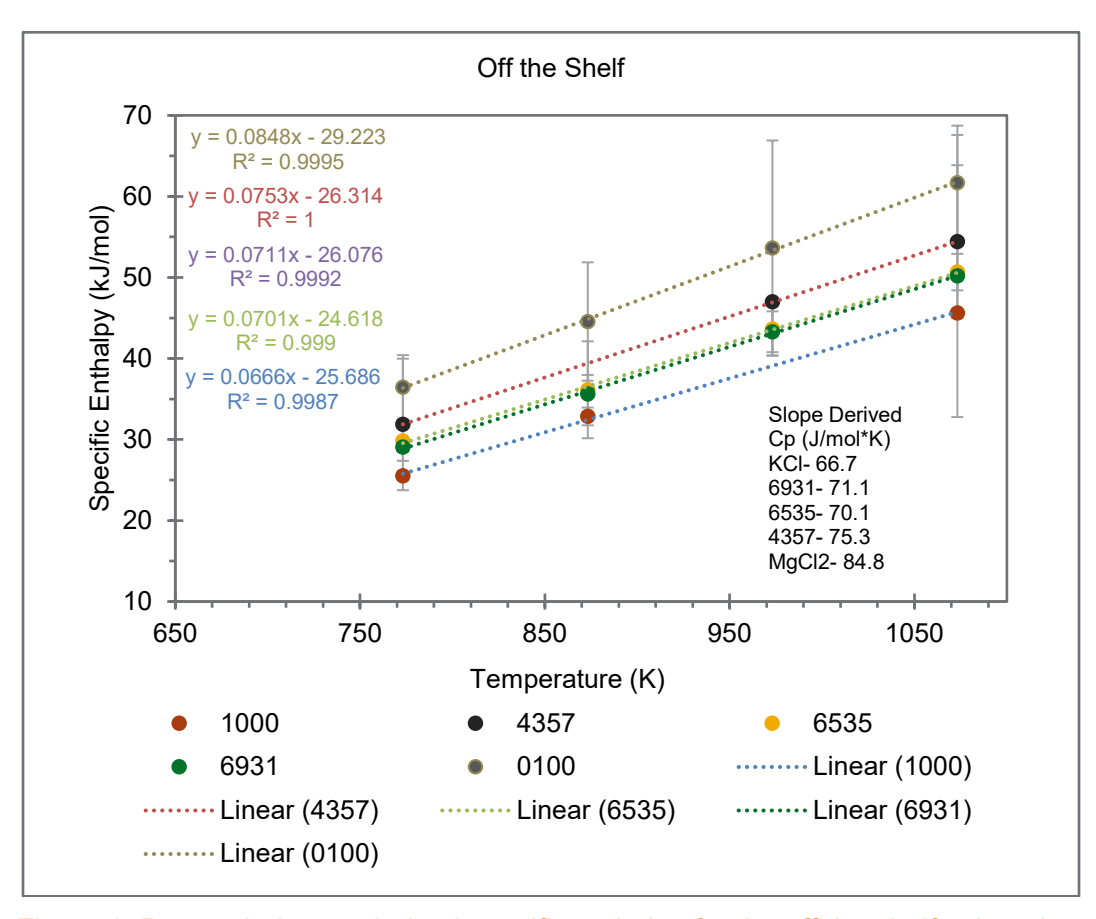


Figure 6. Drop calorimetry derived specific enthalpy for the off the shelf salt series.

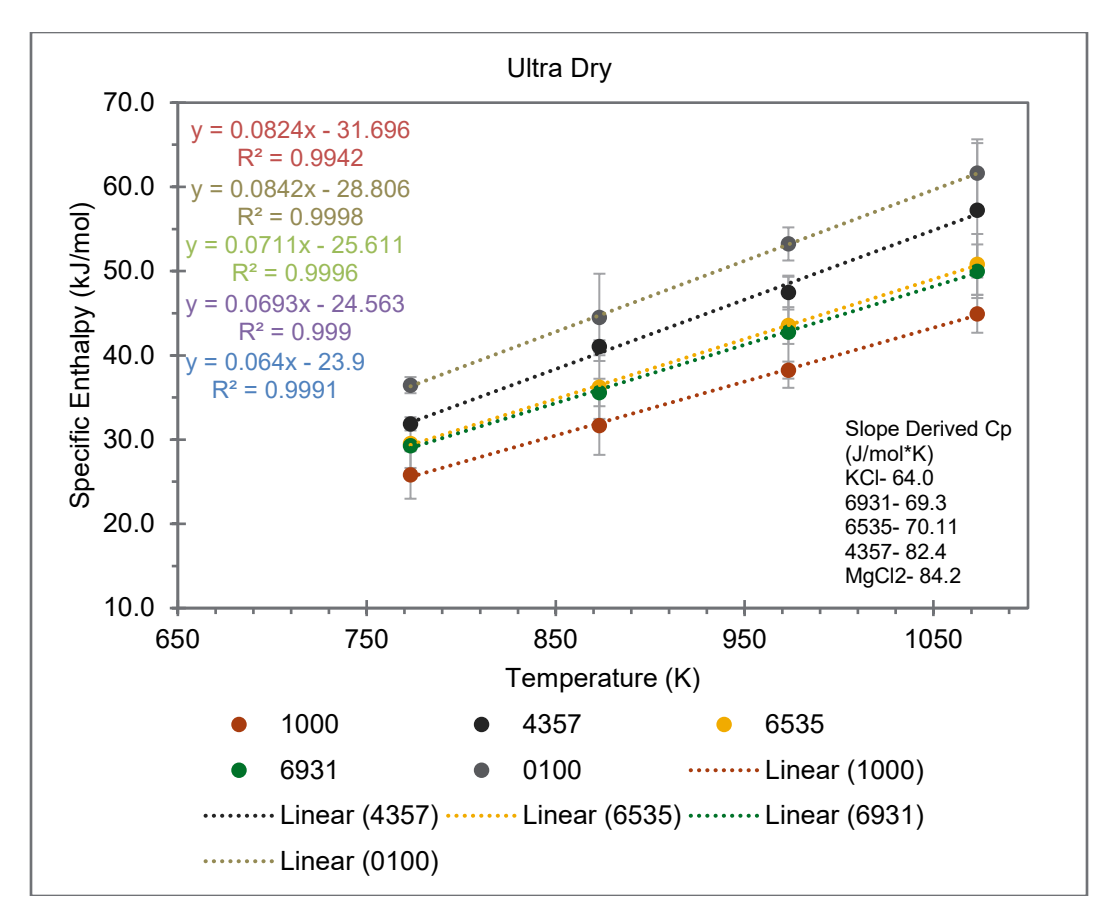


Figure 7. Drop calorimetry derived specific enthalpy for the ultra-dry salt series.

Both 69 and 65 mol% KCl containing 1 wt% of water had notably higher heat capacities than the ultra-dry and for the off the shelf salts. The mixture containing 43 mol% KCl was lower than the ultra-dry salts but elevated compared to the off-the-shelf salts (Figure 8).

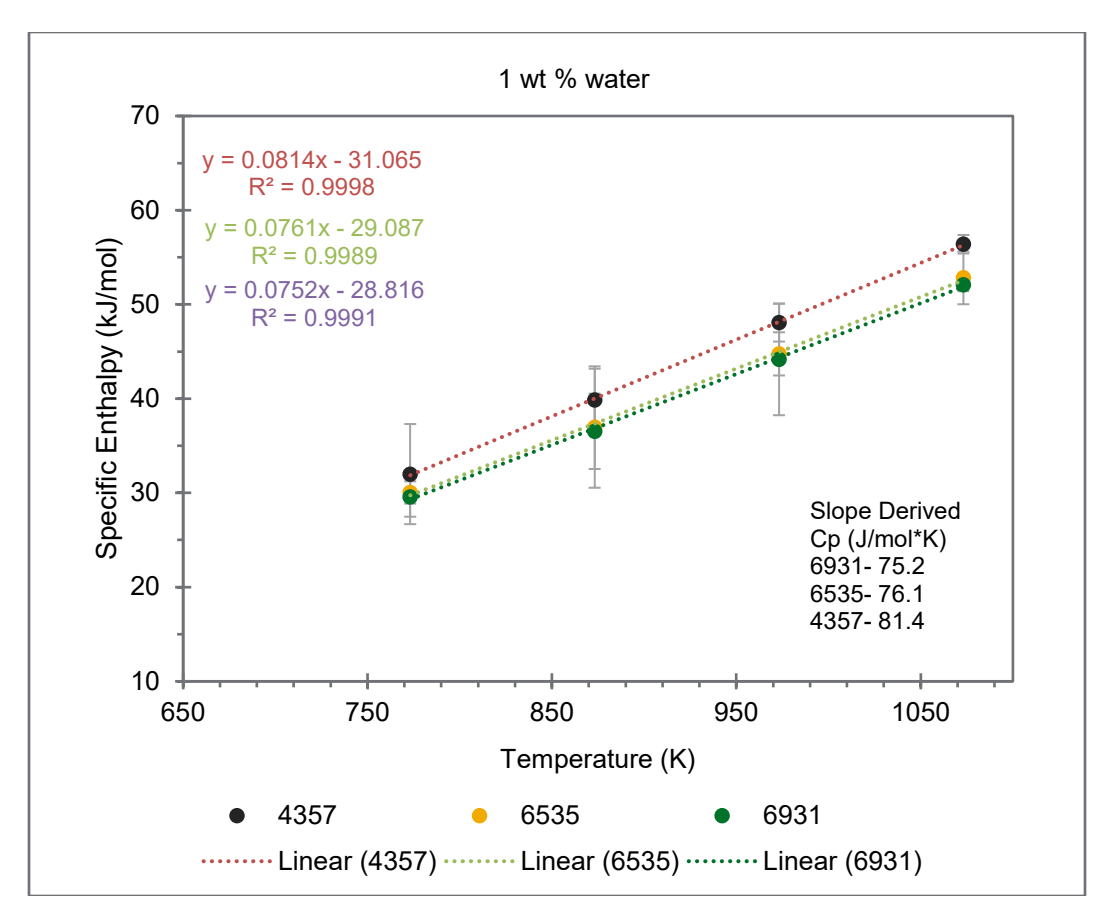


Figure 8. Drop calorimetry derived specific enthalpy for ultra-dry salts doped with 1 wt% water.

At higher heat capacities the material is considered more efficient for the heat exchanger. High water content could potentially lead to other complications. For example the rate of crucible failure amongst the high-water content samples approached 50%, evidence of increased corrosivity of water-bearing molten salts.

The 300 and 600 ppm trace impurity salts were also observed to breach the weld of the nickel crucibles and leak, more frequently at higher temperatures. Heat capacity and specific enthalpy values were determined to be more comparable to the off-the-shelf salts possibly due to the metal basis and manufacture impurities (Figures 9 and 10). The preliminary hypothesis can be concluded that water and trace impurities may have enough impact upon the system in question to warrant more refined analysis.

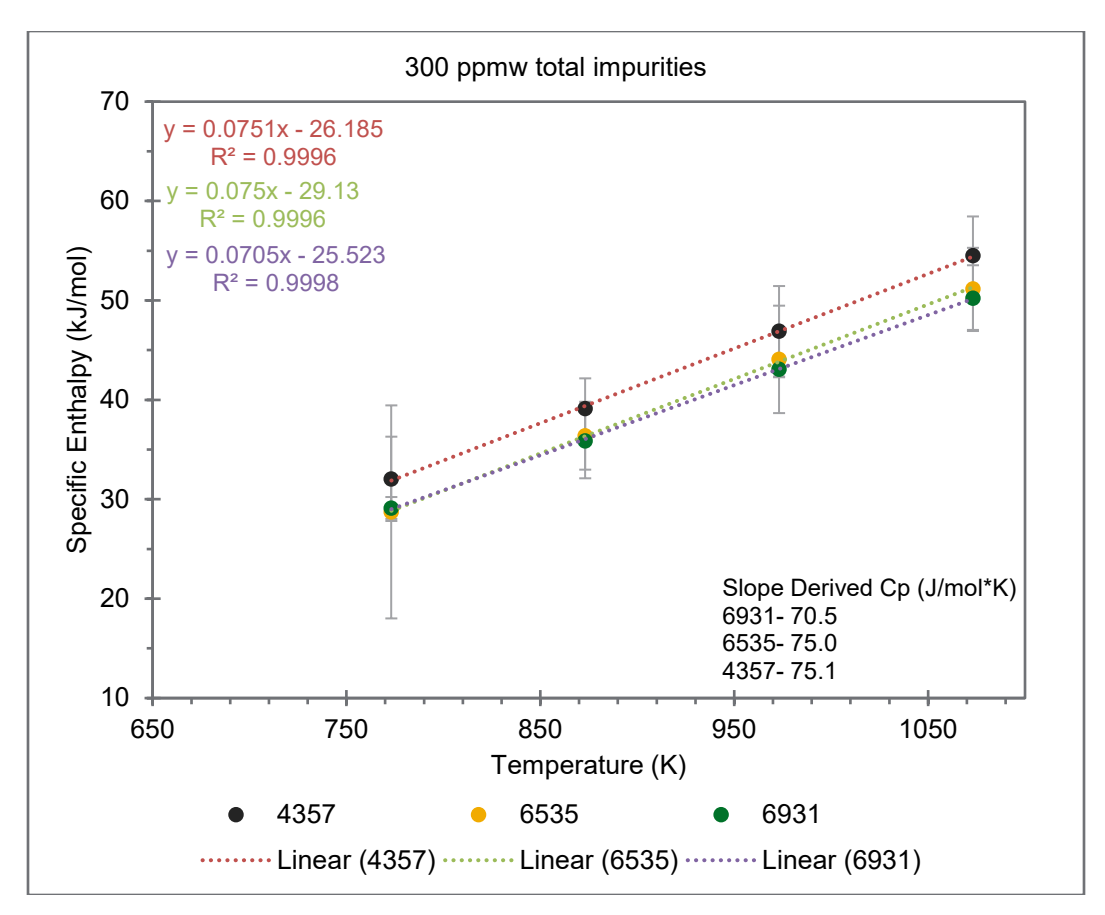


Figure 9. Drop calorimetry derived specific enthalpy for ultra dry salts doped with 300 ppm by weight of Fe, Cr, and Ni.

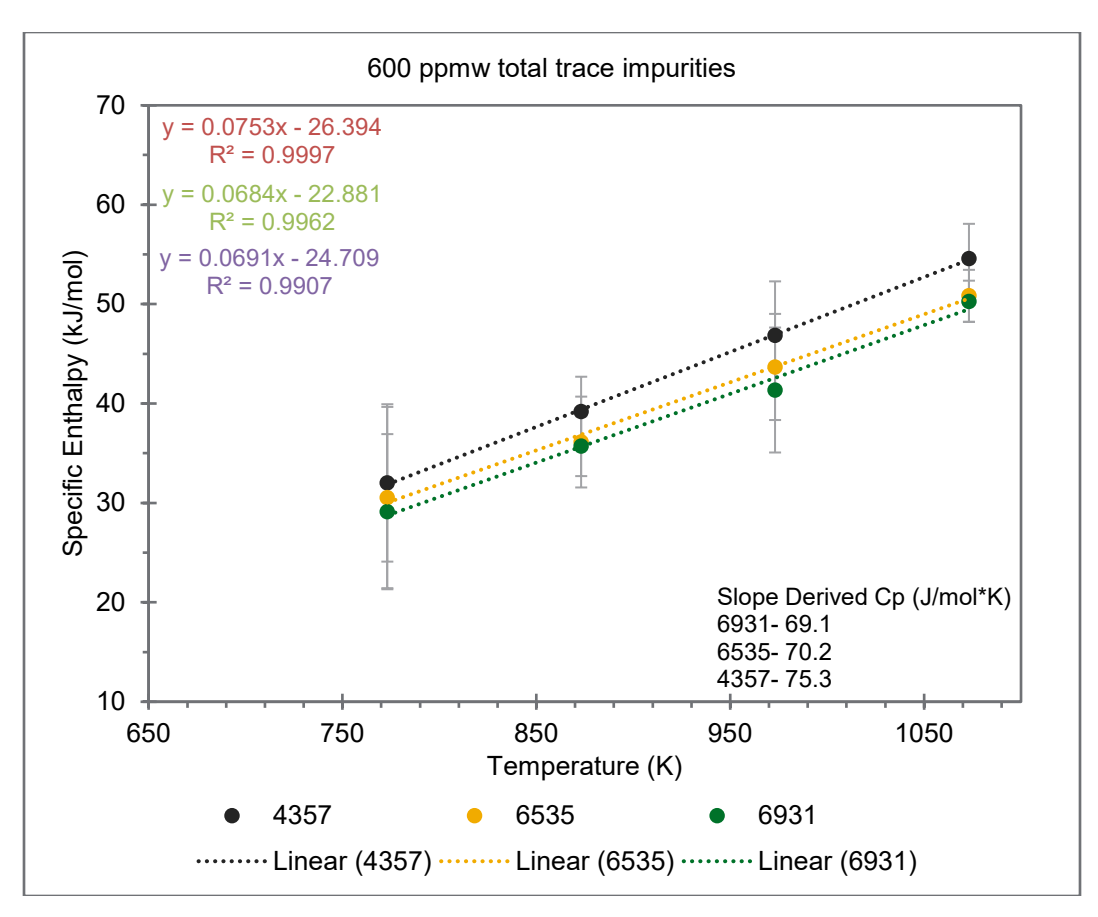


Figure 10. Drop calorimetry derived specific enthalpy for ultra dry salts doped with 600 ppm by weight of Fe, Cr, and Ni

Table 2. Tabulated results of specific enthalpy data determined by drop calorimetry. Mean values have units of kilojoules per mole (kJ/mol). n.d.- not determined.

Series	Temp (K)	KCI		6931		6535		4357		MgCl <sub>2</sub>	
		mean	sd	mean	sd	mean	sd	mean	sd	mean	sd
Off-the-Shelf	673.15	20.4	0.5	22.9	0.6	23.3	2.4	25.0	8.1	28.6	4.0
Off-the-Shelf	773.15	25.5	1.1	29.0	2.4	29.8	6.0	31.9	0.4	36.4	7.3
Off-the-Shelf	873.15	32.8	1.3	35.6	2.5	36.1	3.3	n.d.	n.d.	44.6	13.3
Off-the-Shelf	973.15	n.d.	n.d.	43.3	17.4	43.6	2.3	47.0	9.4	53.6	7.0
Off-the-Shelf	1073.15	45.6	3.1	50.2	2.9	50.7	2.1	54.4	4.1	61.7	4.1
Ultra Dry	773.15	773.2	25.8	29.3	2.6	29.5	0.3	31.9	8.0	36.5	1.0
Ultra Dry	873.15	873.2	31.7	35.6	1.6	36.2	3.8	41.1	0.7	44.5	5.2
Ultra Dry	973.15	973.2	38.3	42.7	6.6	43.5	2.2	47.5	2.0	53.2	2.0
Ultra Dry	1073.15	1073.2	44.9	50.0	3.2	50.8	3.6	57.2	8.0	61.6	4.0

Water Content	773.15	n.d.	n.d.	29.6	2.1	30.0	1.2	32.0	5.3	n.d.	n.d.
Water Content	873.15	n.d.	n.d.	36.5	4.0	37.0	6.4	39.9	3.3	n.d.	n.d.
Water Content	973.15	n.d.	n.d.	44.2	5.9	44.8	2.3	48.1	2.0	n.d.	n.d.
Water Content	1073.15	n.d.	n.d.	52.1	0.7	52.8	2.8	56.4	1.0	n.d.	n.d.
300 ppmw impurities	773.15	n.d.	n.d.	29.1	1.1	28.7	10.7	32.1	4.2	n.d.	n.d.
300 ppmw impurities	873.15	n.d.	n.d.	35.9	3.8	36.4	3.4	39.1	3.0	n.d.	n.d.
300 ppmw impurities	973.15	n.d.	n.d.	43.1	8.0	44.1	5.4	46.9	4.6	n.d.	n.d.
300 ppmw impurities	1073.15	n.d.	n.d.	50.2	3.3	51.2	4.1	54.5	3.9	n.d.	n.d.
600 ppmw impurities	773.15	n.d.	n,d.	29.1	7.8	30.5	9.1	32.0	7.9	n.d.	n.d.
600 ppmw impurities	873.15	n.d.	n,d.	35.7	3.0	36.1	4.6	39.2	3.5	n.d.	n.d.
600 ppmw impurities	973.15	n.d.	n,d.	41.4	6.3	43.7	5.3	46.9	5.4	n.d.	n.d.
600 ppmw impurities	1073.15	n.d.	n,d.	50.3	2.1	50.8	2.6	54.6	3.5	n.d.	n.d.

### 3.2.2 Density

Density is a fundamental property of materials and plays a significant role in MSR design and operation. However, experimental determination of density is challenging because of the corrosive nature and low viscosity of the molten material. To the author's knowledge, no commercial off-the-shelf crucible for the instrument used is available. As was mentioned above, two crucible types were designed and fabricated for this work.

Testing began on the 43 mol% KCl binary mixture. The salts were prepared and analyzed as described above. Figure 11 presents the results from the first test. A starting value of 2.175 g/cm³ was input for density at room temperature. The black curve in Figure 11 represents the height change recorded by the instrument during the experiment. From room temperature to ~440 °C, the slope of the dL/L₀ curve is quasi-linear, representing a steady increase in the height of the plunger due to the linear thermal expansion of the solid salt mixture. An inflection in the slope occurs at approximately 383 °C and may be associated with a phase change or dehydration reaction. The onset of melting is delineated by the sharp change in slope in the dL/L₀ curve beginning at 444 °C, with complete melting occurring by 477 °C. This temperature is in excellent agreement with previous workers (470 °C; Perry and Fletcher, 1992), providing a secondary confirmation independent of the LIBS results for correct batched ratios. At the onset of melting, a sharp change in slope is observed in the density (blue) curve in Figure 11. At the

completion of melting, the curve from 477 °C to 800 °C is calculated using Equation 3. Density decreases from 2.077 to 2.042 g/cm³ in this temperature range.

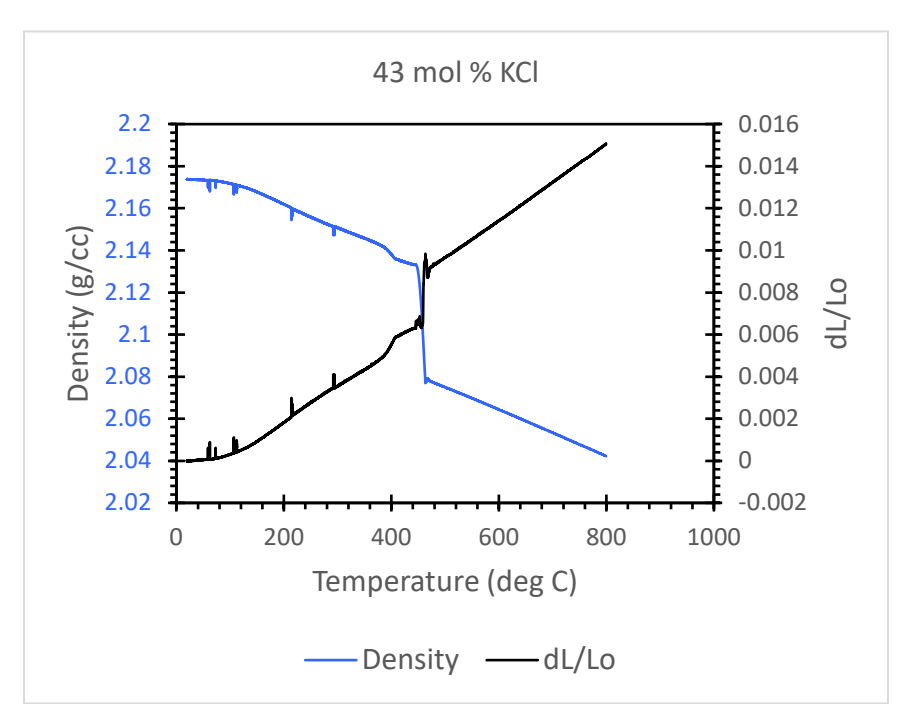


Figure 11. Experimentally derived density curve for the 43 mol % KCl mixture between room temperature and 800 °C.

Classical Molecular Dynamic (CMD) and ab initio Molecular Dynamic (AIMD) modeling are often employed to better understand the fundamental properties of various materials, including molten salts. In the same FY as this group focused on the experimental determination of density for the KCI-MgCl<sub>2</sub> system, another group at PNNL was utilizing these modeling techniques for the same system. This provided an excellent point of comparison between the two methods. Modeled and experimental results are summarized in Table 3. One will notice the TMA results are consistently high compared to the two modeled results. Several details must be considered when comparing these results. Likely the most significant detail is the modeled densities are determined on completely pure compounds. The LIBS data produced for the salts used in the experiments showed evidence of impurities, e.g., H and O (section 3.1), Another consideration is the change in dL/L<sub>o</sub> over the course of the experiment only changes by 0.016 which translates to a total height change of 457 µm. Even a minuscule perturbation during measurement could significantly impact the results. Lastly, a small amount of salt was observed on the crucible after a replicate run was completed. If this salt was lost during the experiment, it would decrease the volume in the crucible thereby decreasing the total height of the plunger and ultimately resulting in a higher apparent density. Despite this, the similarity between the experimentally derived and modeled results showed promise for the efficacy of the method.

Table 3. Comparison of densities derived by experimental (this work) and molecular dynamic modeling. Values in this table have units of grams per cubic centimeter (g/cm3).

\*Density values from personal communication with Manh Nguyen, 2024.

Temp C	TMA	CMD*	AIMD*
445	2.13		
500	2.07		
600	2.06	1.90	1.69
700	2.05	1.87	1.67
800	2.04	1.85	1.62

Experimentation continued with the 65 and 69 mol% KCl salt mixtures. Each experiment was conducted using the same parameters and crucibles. After several attempts, it proved nearly impossible to prevent the salt from escaping the crucible during the experiment. This is usually evidenced in-process by a sudden and sustained drop in the  $dL/L_{\circ}$  curve. Because of this, it was decided to invest effort into the design of a different crucible type.

Alumina was chosen as the material of interest for the second crucible design. As was mentioned in section 2.3.2, two crucibles were fabricated with plunger outer diameters of 7.880 and 7.900 mm, with the crucible base containing an inner diameter of 8.000 mm. Salt leakage was observed with these crucibles, albeit less extensive than those with the nickel crucibles. After several attempts, work ceased on this crucible design. No reportable data were produced with these crucibles.

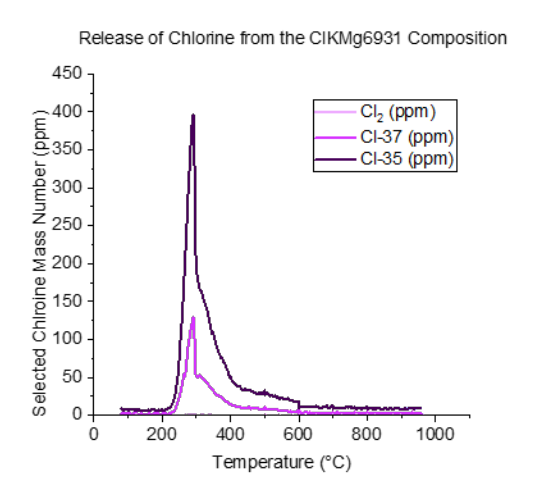
Research into a third crucible design has been undertaken. Unlike the previous two iterations, several other material characteristics were considered in addition to its coefficient of thermal expansion. A detailed discussion is beyond the scope of the main text here; however, the new crucible design is presented in full detail in Appendix A.

### 3.2.3 Volatility

Vapor pressure and volatility can be considered the most crucial for thermal hydraulic design and reactor operation. An increase in vapor pressure has the potential to increase pressure within the core that could lead to a pressure related incident. If pressure needs to be stopped and released during reactor operation, the off-gas and speciation of the salts being released must be understood to ensure safe release of pressure. The volatility can affect the molar ratio of the salts in the system which will then complicate the thermal hydraulic calculation as the salt

is no longer the original composition. A critical change in molar ratio can disrupt the void and thermal coefficients which can lead to a higher risk of an uncontrolled reaction.

Preliminary experiments were conducted with an EGA to try and determine the off-gas species during the melt of the salt. Though the EGA is an excellent instrument for determining released gas from the salts, the evaporated salt would plate out and clog the sample transfer line prior to reaching the instrument detectors even with the high carrier gas flow. The hypothesis is the heated capillary tube within the sample transfer line is maintained too low, at 100 °C, to keep the evaporated salts from plating to the walls. Unfortunately, the experiments conducted did not lead to any significant findings, however, the EGA did provide an interesting observation. Off-the-shelf 69 mol% KCl produced a chlorine spike at 300 °C that occurred during a ramping portion of the testing parameters rather than at the predicted isothermal hold (Figure 12).



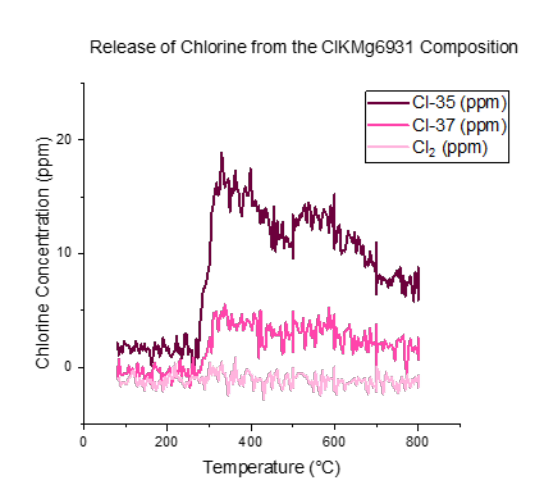


Figure 12. Selected chlorine mass number release from 69 mol % KCl mixture; Left) same mixture ran in December. Samples derived from off-the-shelf salts. Right) 69 mol % ran in January taken from the ultra-dry batch prepared day of experiment in glovebox.

Off-the-shelf 69 mol% KCl did not melt at the anticipated melting point of ~423°C and was still in a solid phase past the melting point of KCl (770°C). The working hypothesis is chlorine is released from the solid, allowing for an oxidation reaction to occur and convert the free magnesium into magnesium oxide. For this reaction to occur the following criteria for the chemical equation need to be met:

$$MgCl_{2(s)} + H_2O_{(l)} \rightarrow MgO_{(s)} + 2HCl_{(g)}$$
 (Eqn. 4)

This led to the testing of the ultra-dry pure MgCl<sub>2</sub> to determine if hydrochloric gas was being released alongside chlorine gas. Figure 12 confirms the release of both hydrochloric and chlorine gas releasing at low temperatures during the ramping of the furnace which then allows for the conditions to be met to convert MgCl<sub>2</sub> to magnesium oxide (MgO). Since the EGA was unable to identify if any salt was being released the lack of data produced from the EGA led to the use of XRD to determine if the conversion was occurring.

In the exploratory stages of the XRD experiments, the main purpose was to compare peak ratios between the starting material from the source container and samples that had undergone EGA experiments to determine how much of the salt was released. However, with hygroscopic

behavior of the MgCl<sub>2</sub>, the salts expanded and formed a crust layer, which prevented a diffraction angle from being collected under ambient atmosphere. Therefore, a non-ambient, hot stage was used to heat the sample and collect characterization spectra at different temperatures. The hot stage allowed to collect indirect volatility information.

Figure 13 shows the peak at  $40~2\theta$  is from the platinum plate sample holder of the hot stage XRD. This is likely due to the beam path not being level with the sample stage. The platinum sample plate interference caused a slight shift in the peaks and the platinum to be detected (Figure 13).

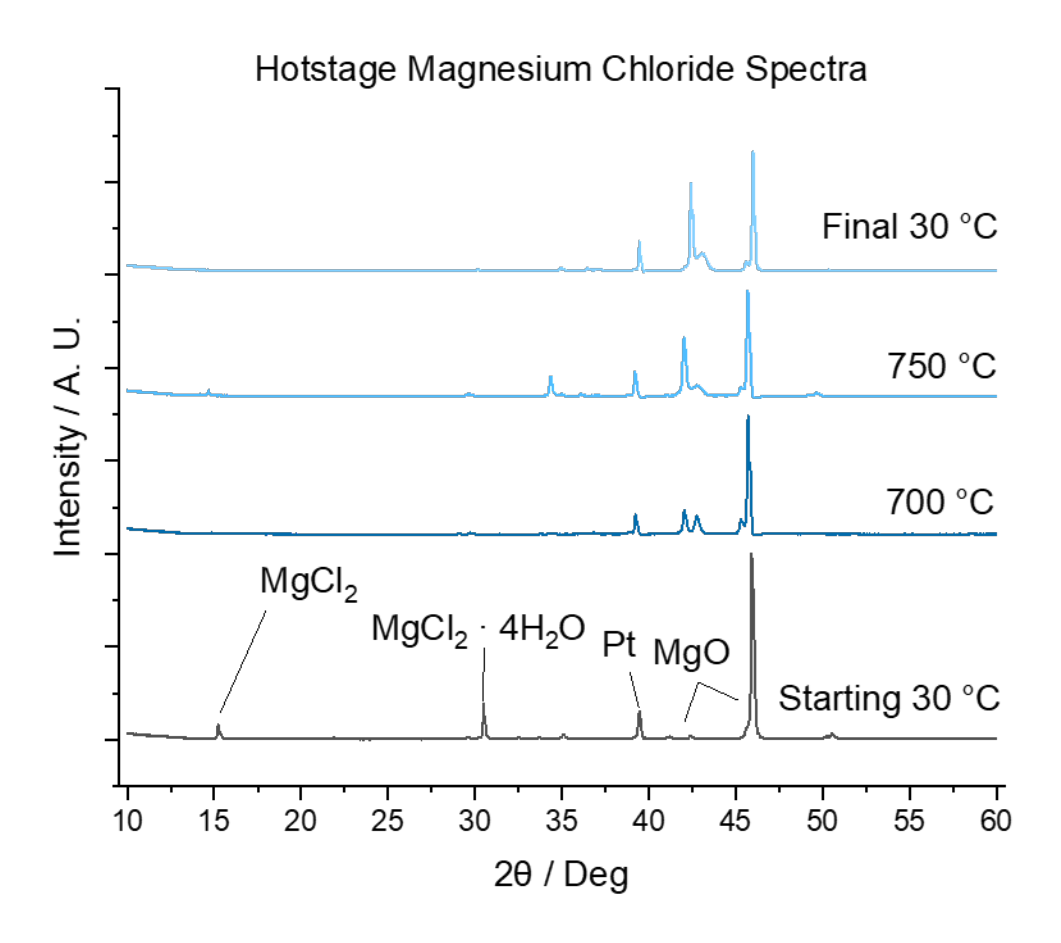


Figure 13. Hot stage XRD results of MgCl<sub>2</sub> at target temperatures.

The pellet was pressed in the glovebox and then transferred with minimal exposure to the atmosphere before being placed on the sample holder and sealed in the chamber. The starting scan showed a large amount of MgO and KMgCl<sub>2</sub>·4H<sub>2</sub>O compared to MgCl<sub>2</sub>. One explanation is the source material contained trace contaminants that are likely not evenly dispersed in the container. Another observation from the heated scans is that the MgCl<sub>2</sub> appears to fully convert to MgO, and the change occurs prior to the melting point. The eutectic composition 43 mol% KCl was chosen because it has the most even distribution of both endmembers with a slightly higher concentration of MgCl<sub>2</sub>. This was to test if the MgCl<sub>2</sub> favored a reaction with KCl over the conversion to MgO. During the starting scan at 30 °C, there are peaks indicating the presence of Mg and K (Figure 14).

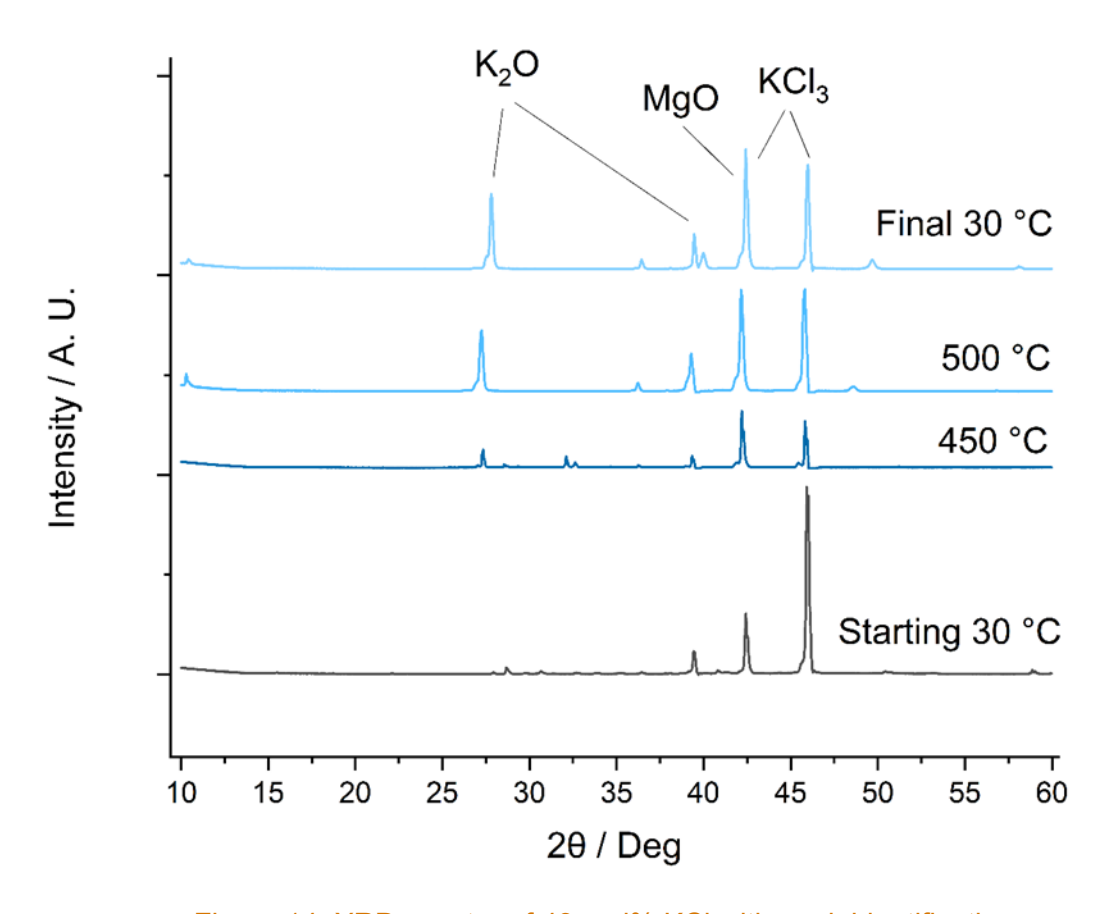


Figure 14. XRD spectra of 43 mol% KCl with peak identification.

The sample source material from which the 43 mol% KCl sample was drawn, was confirmed to be the correct ratio of  $MgCl_2$  to KCl. The assumption can be made that the diffraction beam for the starting spectra did not have  $MgCl_2$  in the preferred orientation to produce the peak. Subsequent peaks are presented in the later spectra. Potassium oxide and KCl<sub>3</sub> structures were present as temperature increased.

The statement can then be made, partnered with the results from the EGA experiments, that the chloride being released from the compound prior to the melting point is allowing the chemical reaction to take place and convert the ions of  $Mg^{2+}$  and  $K^+$  to readily take up any oxygen from atmospheric water or trace contaminants in the salts themselves. Carbon tape was used to pick up subsamples of the vapor trail and analyzed with LIBS and a scanning electron microscope energy-dispersive X-ray spectroscopy (SEM-EDS). Opening the sample chamber resulted in a rapid exposure to air after being held in helium and the vapor trails started to deliquesce, even when transferred to the carbon tape. Samples were taken quickly and then immediately stored in either a desiccator or glovebox and sealed in an inert environment before being transferred for analysis. LIBS and SEM analysis indicated that  $MgCl_2$  was emanating off as a vapor during the heating cycle.

Figure 15 shows a distinct vapor trail that was released from the pellet during the experiment.

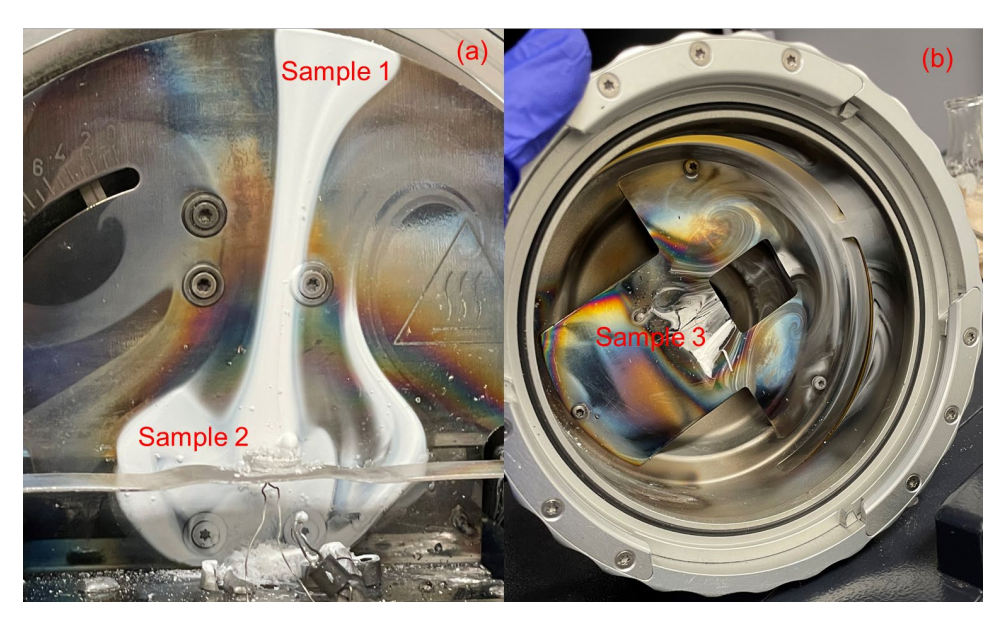


Figure 15. Vapor trail from MgCl<sub>2</sub> after completed scan (a) the back of the sample holder with subsamples collected from labeled sections (b) front of sample holder with a subsample taken from labeled section.

This vapor release was significant and resulted in low sample recovery. Once the resulting vapor trail was exposed to the atmosphere, it immediately began deliquescing. The material was subsampled (Fig. 15) and analyzed via XRD and LIBS. The results suggested a chloride phase was present in the vapor. This discovery led to the development of a method whereby this vapor could be created and collected in a controlled manner.

The concept of utilizing a cold trap to capture volatilized salt was devised upon observation of the vapor trail in the hot-stage XRD experiments. There is a question in the molten salt community regarding the volatile nature of molten chloride and fluoride salts. The observation of the vapor trail in the XRD experiments is at minimum confirmation that at least the KCI-MgCl<sub>2</sub> system is volatile. Confirming volatility alone, however, is not enough. The goal of the cold trap experiments was to capture both the condensate and residual fractions and characterize their chemical composition and crystal structure to better understand the nature of the volatility. Accurate models of the behavior of molten salts in a reactor fundamentally rely on knowledge of the composition of that salt. Incongruent volatilization would lead to an evolving composition of the remaining melt through time. If this is not accurately included in such models, a fundamental flaw exists which may lead to either under-informed interpretations about the efficacy of a salt mixture or in a worst-case scenario, lead to unaccounted hazards for which the reactor is not designed.

In total twelve CT-CPA tests were conducted across four compositions. These include the three eutectic compositions of 43, 65, and 69 mol % KCl and a fourth composition consisting of 69 mol % KCl doped with 300 ppm total impurities (by weight) of Fe, Ni, and Cr. Each composition was tested in triplicate with the exception of the trace impurities compositions, which were only tested in duplicate. The results presented here are not exhaustive but instead summarized by a few key points. The full data set and resulting conclusions are intended to be included in a peer-reviewed manuscript in the near future.

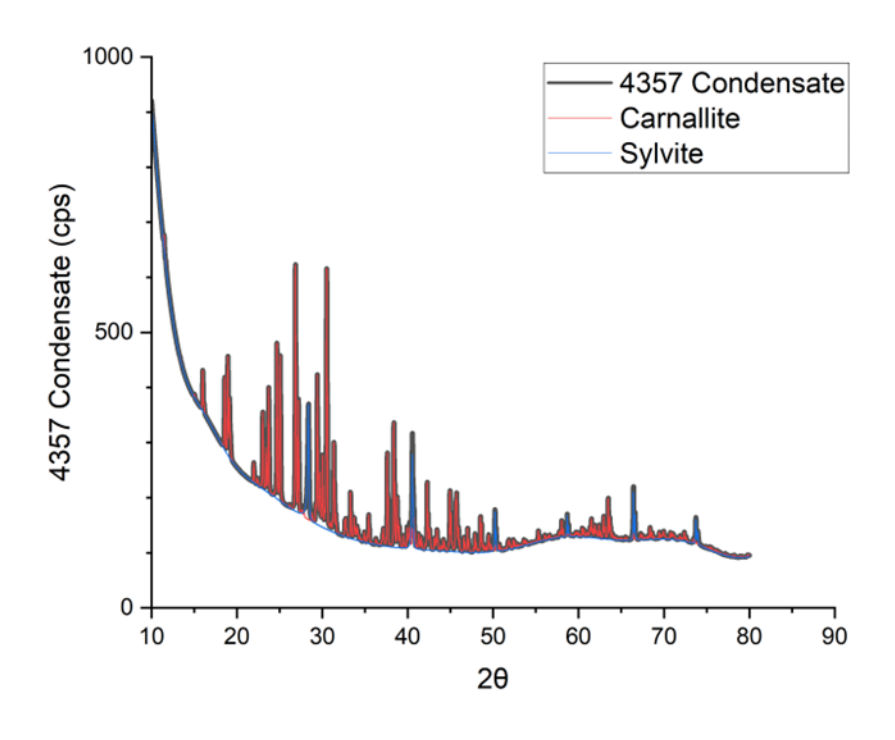
\*NOTE\* Extreme care must be taken when using this methodology as a significant burn hazard exists when removing the cold trap tube from the furnace. As was mentioned in section 2.3.3.3, all experiments were conducted at 850 °C, and samples were held at this temperature for 120 minutes. At the end of the isothermal hold, both the furnace and chiller are de-energized, and the coolant flow tubes are removed from the ends of the cold trap tube. Both compression fittings are removed, and the cold trap tube is then carefully removed from the tube furnace. This must be executed in a safe and efficient manner, otherwise the cold trap tube may heat past the melting point of the salt, causing sample loss. Figure 16 shows the result of the first cold trap experiment. As expected based on the observations from Figure 15, a significant amount of salt had volatilized and condensed onto the cold trap.



Figure 16. Photograph taken of the cold trap after the initial test run. The white substance is the condensed salt vapor. Length of cold trap tube visible in this photograph is approximately 200 mm.

Condensate and residue fractions were characterized by XRD. In many cases, a small subsample (~10 mg) of salt was removed from the cold finger directly onto a low-background XRD sample holder and immediately analyzed. For those samples that were not immediately analyzed, care was taken to remove the condensate fractions from the cold trap tube and transfer them to an inert atmosphere glovebox, where they were stored until the XRD analysis.

For the 43 mol% KCl mixture (Fig. 17), carnallite (KMgCl<sub>3</sub>) and pure KCl are present as crystal phases in both fractions, a feature unique to this eutectic mixture. Spectral analysis reveals carnallite consists of 78% of the condensate fraction, with the balance being KCl (Table 4). Based on stoichiometry and mass balance this equates to total K in the condensate fraction of 61%, suggesting the condensate is enriched in K relative to the starting 43 mol% composition.



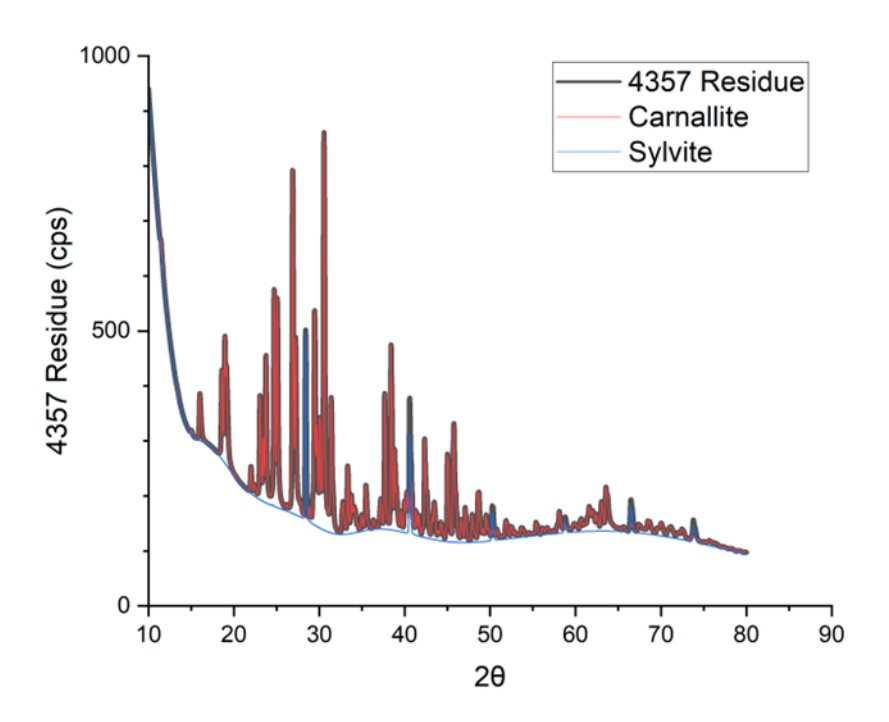
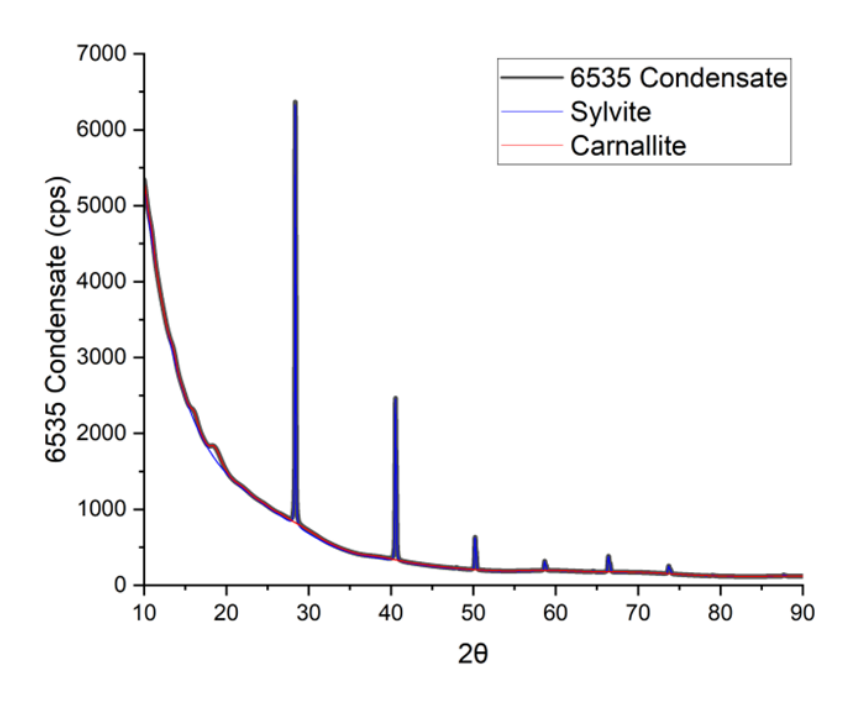


Figure 17. X-ray diffraction patterns for condensate and residue fractions from the 43 mol% KCI mixture.

For the 65 mol% KCl mixture (Fig. 18), carnallite and KCl are present in the condensate fraction, whereas the crystalline phases identified in the residue fraction are KCl and MgCl<sub>2</sub>. Spectral

analysis reveals carnallite consists of 69.1% of the condensate, with the balance being KCI (Table 4). Again, using stoichiometry and mass balance, the total K in the condensate fraction equates to 65.45%, very close to the starting composition of 65 mol%. This is the only example of the twelve runs exhibiting what appears to be congruent volatilization.



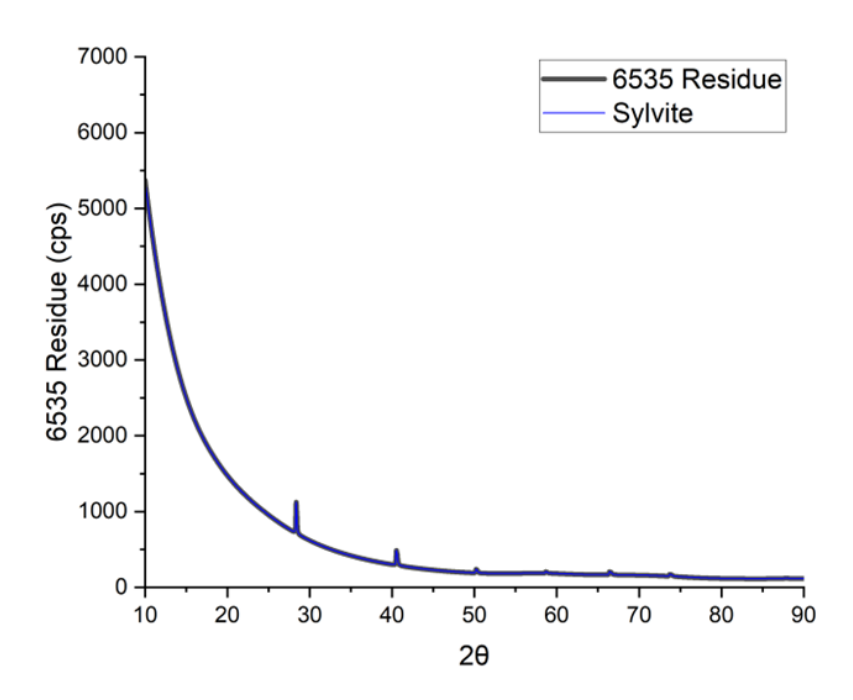
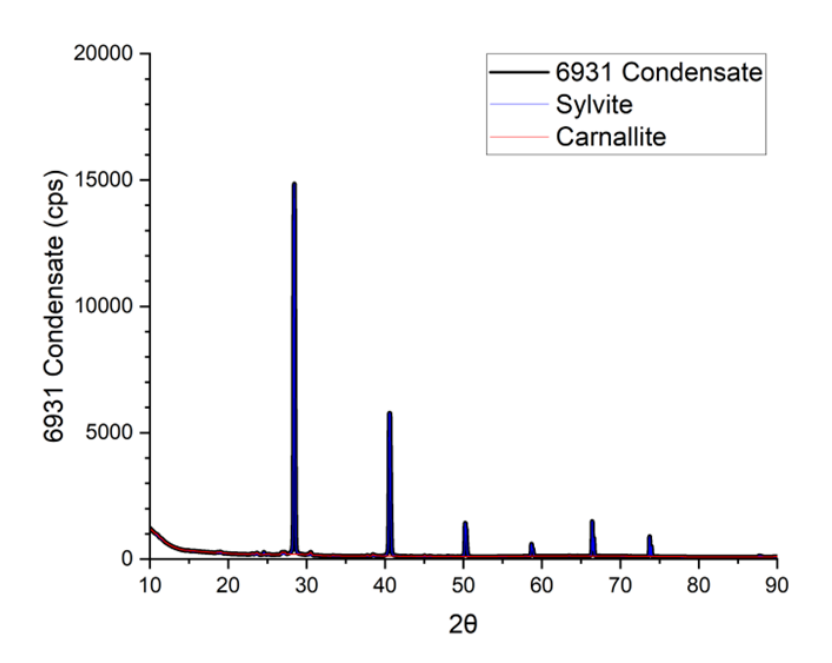


Figure 18. X-ray diffraction patterns for condensate and residue fractions from the 65 mol% KCI mixture.

For the 69 mol% mixture (Fig. 19), both carnallite and KCI were identified in the condensate fraction, accounting for 11.6 and 88.4%, respectively (Table 4). Using stoichiometry and mass balance, this equates to a total K content of 94.2% in the condensate fraction and represents the largest deviation observed from its starting composition.



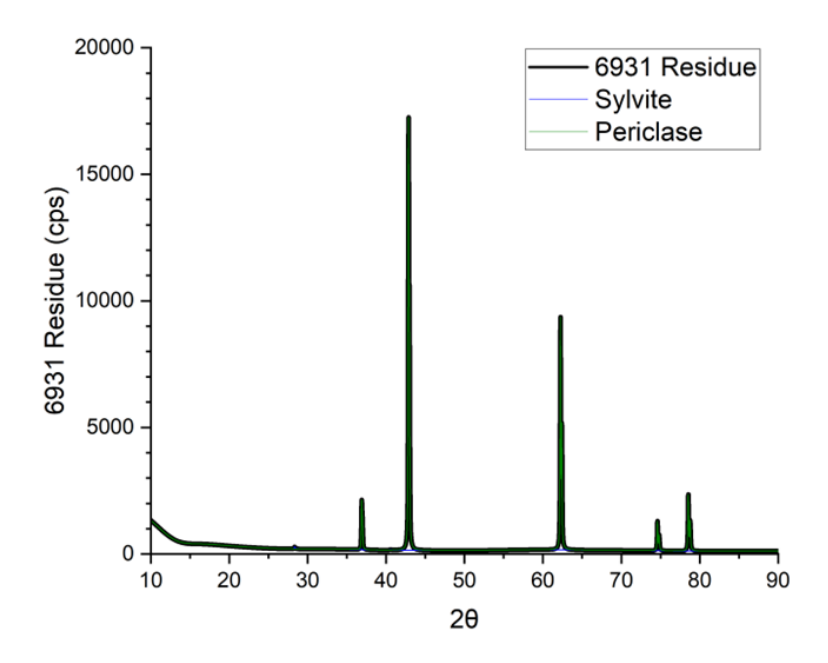
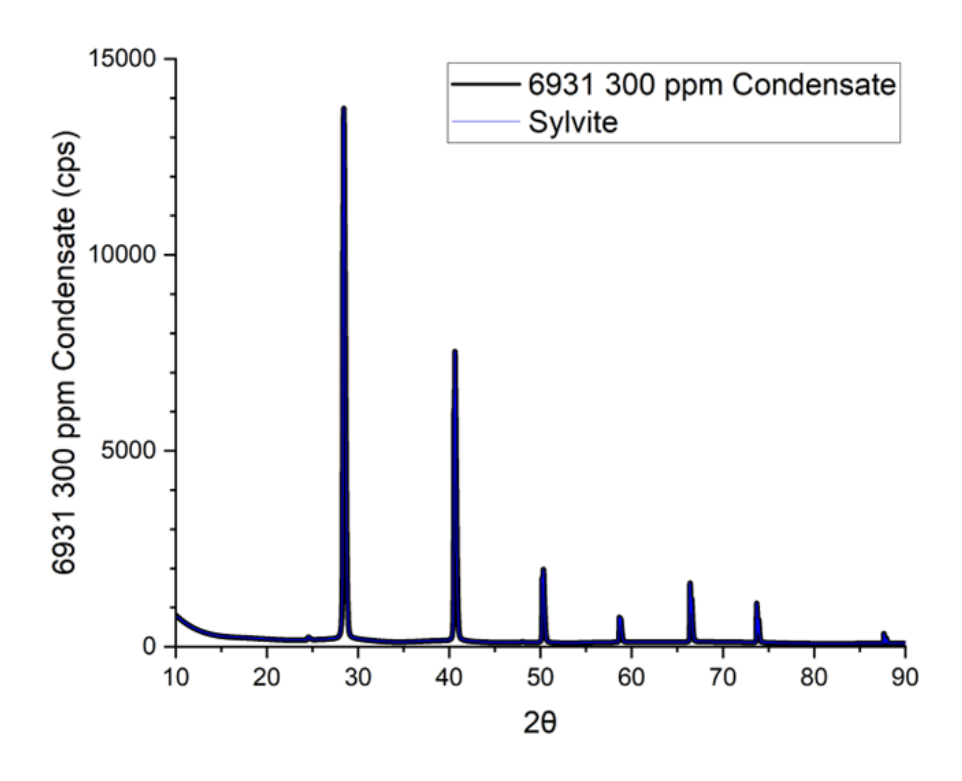


Figure 19. X-ray diffraction patterns for condensate and residue fractions from the 69 mol% KCI mixture.

For the 69 mol% mixture with 300 ppm Fe, Cr, and Ni (Fig. 20), only KCl was identified in the condensate fraction and interestingly, only periclase (MgO) was identified in the residue fraction (Table 4). Importantly, no Fe, Ni, or Cr crystalline phase was identified in the condensate or residue fraction. At this time, the reason behind the residue fraction containing only an oxide phase is unclear, as sample preparation, handling, the volatility experiment, and analysis were identical to previous runs. However, it is possible, despite thoughtful efforts to minimize O contamination during the volatility experiment, that a leak was present allowing for the infiltration of O into the system. Another possibility is with the impurities themselves. The source material for the Fe, Cr, and Ni phases were iron chloride (FeCl<sub>2</sub>), chromium chloride (CrCl<sub>2</sub>), and nickel chloride (NiCl<sub>2</sub>). These starting chlorides were not tested by Karl Fischer for their moisture content nor were they analyzed by LIBS for their impurity content. Future work will address this potential pitfall.



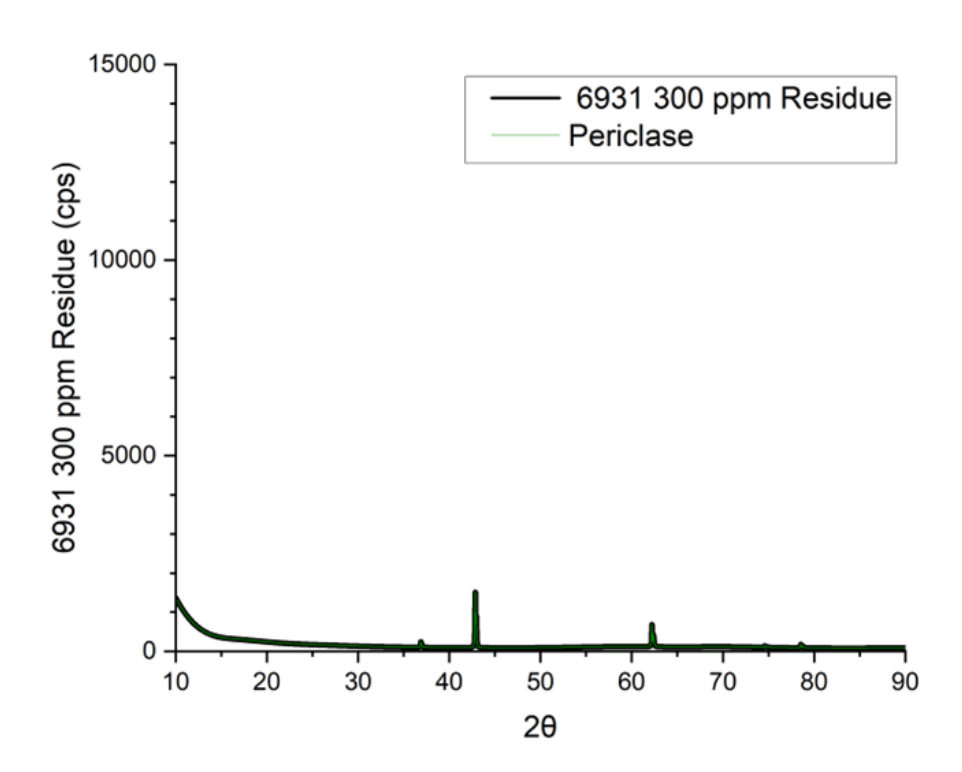


Figure 20. X-ray diffraction patterns for condensate and residue fractions from the 69 mol% KCl mixture doped with 300 ppm by weight Fe, Cr, and Ni.

Table 4. Phases and their percentage compositions in residue and condensate fractions for select runs determined by XRD analysis.

Salt	Fraction	KMgCl	KCI	MgCl2	MgO
4357 t1	Condensate	78.1	21.9		
4357 t1	Residue	96	4		
6535 t3	Condensate	69.1	30.9		
6535 t3	Residue		55.9	44.1	
6931 t4	Condensate	11.6	88.4		
6931 t4	Residue		0.26		99.74
6931 t2 300	Condensate		100		
ppm					
6931 t2 300 ppm	Residue				100

As the starting composition moves from unity the condensate fraction becomes more enriched in KCI. It is important to note however that XRD is only sensitive to the crystalline phases present in the sample. It is reasonable to expect that given the near quenching conditions the samples experience at the end of the experiment, some of the samples are amorphous. To better understand this, subsamples were prepared for imaging and chemical composition analysis via SEM-EDS.

Condensed solids on the cold trap are very fine-grained. While removing the material from the cold trap, a small amount of material would flake off and stay suspended in the air, much like a feather. This initial observation suggested the material was very fine-grained. Unlike the condensate fraction, the residue fraction was often fused to the platinum foil and took considerable effort to remove. When it was liberated, the pieces were often large and appeared to be subhedral to euhedral.

Condensed solids from the 43 mol% starting composition can be seen in Figure 21. Upon first investigation at low magnification, it appears the material is relatively heterogenous in shape and size. However, at higher magnifications, it is clear the actual individual particle sizes are homogenous. Typical grains appear euhedral (well-defined crystallinity) and are in the 0.5-1  $\mu$ m size range. The residue appears blocky at both low and high magnifications with several crystals exhibiting hexagonal morphology. Some double pyramid crystal terminations are evident in a few crystals (see Fig. 21).

# ### 17/2/2024 | Wr | 100 | 100 | 100 | 100 | 100 | 100 | 100 | 100 | 100 | 100 | 100 | 100 | 100 | 100 | 100 | 100 | 100 | 100 | 100 | 100 | 100 | 100 | 100 | 100 | 100 | 100 | 100 | 100 | 100 | 100 | 100 | 100 | 100 | 100 | 100 | 100 | 100 | 100 | 100 | 100 | 100 | 100 | 100 | 100 | 100 | 100 | 100 | 100 | 100 | 100 | 100 | 100 | 100 | 100 | 100 | 100 | 100 | 100 | 100 | 100 | 100 | 100 | 100 | 100 | 100 | 100 | 100 | 100 | 100 | 100 | 100 | 100 | 100 | 100 | 100 | 100 | 100 | 100 | 100 | 100 | 100 | 100 | 100 | 100 | 100 | 100 | 100 | 100 | 100 | 100 | 100 | 100 | 100 | 100 | 100 | 100 | 100 | 100 | 100 | 100 | 100 | 100 | 100 | 100 | 100 | 100 | 100 | 100 | 100 | 100 | 100 | 100 | 100 | 100 | 100 | 100 | 100 | 100 | 100 | 100 | 100 | 100 | 100 | 100 | 100 | 100 | 100 | 100 | 100 | 100 | 100 | 100 | 100 | 100 | 100 | 100 | 100 | 100 | 100 | 100 | 100 | 100 | 100 | 100 | 100 | 100 | 100 | 100 | 100 | 100 | 100 | 100 | 100 | 100 | 100 | 100 | 100 | 100 | 100 | 100 | 100 | 100 | 100 | 100 | 100 | 100 | 100 | 100 | 100 | 100 | 100 | 100 | 100 | 100 | 100 | 100 | 100 | 100 | 100 | 100 | 100 | 100 | 100 | 100 | 100 | 100 | 100 | 100 | 100 | 100 | 100 | 100 | 100 | 100 | 100 | 100 | 100 | 100 | 100 | 100 | 100 | 100 | 100 | 100 | 100 | 100 | 100 | 100 | 100 | 100 | 100 | 100 | 100 | 100 | 100 | 100 | 100 | 100 | 100 | 100 | 100 | 100 | 100 | 100 | 100 | 100 | 100 | 100 | 100 | 100 | 100 | 100 | 100 | 100 | 100 | 100 | 100 | 100 | 100 | 100 | 100 | 100 | 100 | 100 | 100 | 100 | 100 | 100 | 100 | 100 | 100 | 100 | 100 | 100 | 100 | 100 | 100 | 100 | 100 | 100 | 100 | 100 | 100 | 100 | 100 | 100 | 100 | 100 | 100 | 100 | 100 | 100 | 100 | 100 | 100 | 100 | 100 | 100 | 100 | 100 | 100 | 100 | 100 | 100 | 100 | 100 | 100 | 100 | 100 | 100 | 100 | 100 | 100 | 100 | 100 | 100 | 100 | 100 | 100 | 100 | 100 | 100 | 100 | 100 | 100 | 100 | 100 | 100 | 100 | 100 | 100 | 100 | 100 | 100 | 100 | 100 | 100 | 100 | 100 | 100 | 100 | 100 | 100 | 100 | 100 | 100 | 100 | 100 | 100 | 100 | 100 | 100 | 100 | 100 | 100 | 100 | 100 | 100

## Figure 21. Secondary electron images of the condensate and residue fractions for the 43 mol% KCI mixture. All figures containing SEM images are presented in a similar fashion, that is, two images from each condensate and residual fraction, at both a low magnification (1,000-2,000x; left) and high magnification (10,000-20,000x; right).

X-ray emission maps produced by EDS reveal a homogenous distribution of both K and Mg in the condensate fraction (Fig. 22). This is in stark contrast to that in the residue fraction where K and Mg appear to be segregated into mostly discrete areas. There is however homogenous distribution of Cl in the same region. This may speak to the mixing characteristics of molten KCl with MgCl<sub>2</sub> or may be related to phase separation during cooling. There is a clear spatial correlation between Mg and O in the residue fraction, suggesting a MgO phase. Oxygen is more diffuse in the condensate fraction, suggesting general contamination (i.e., impurity) as opposed to an actual discrete phase.

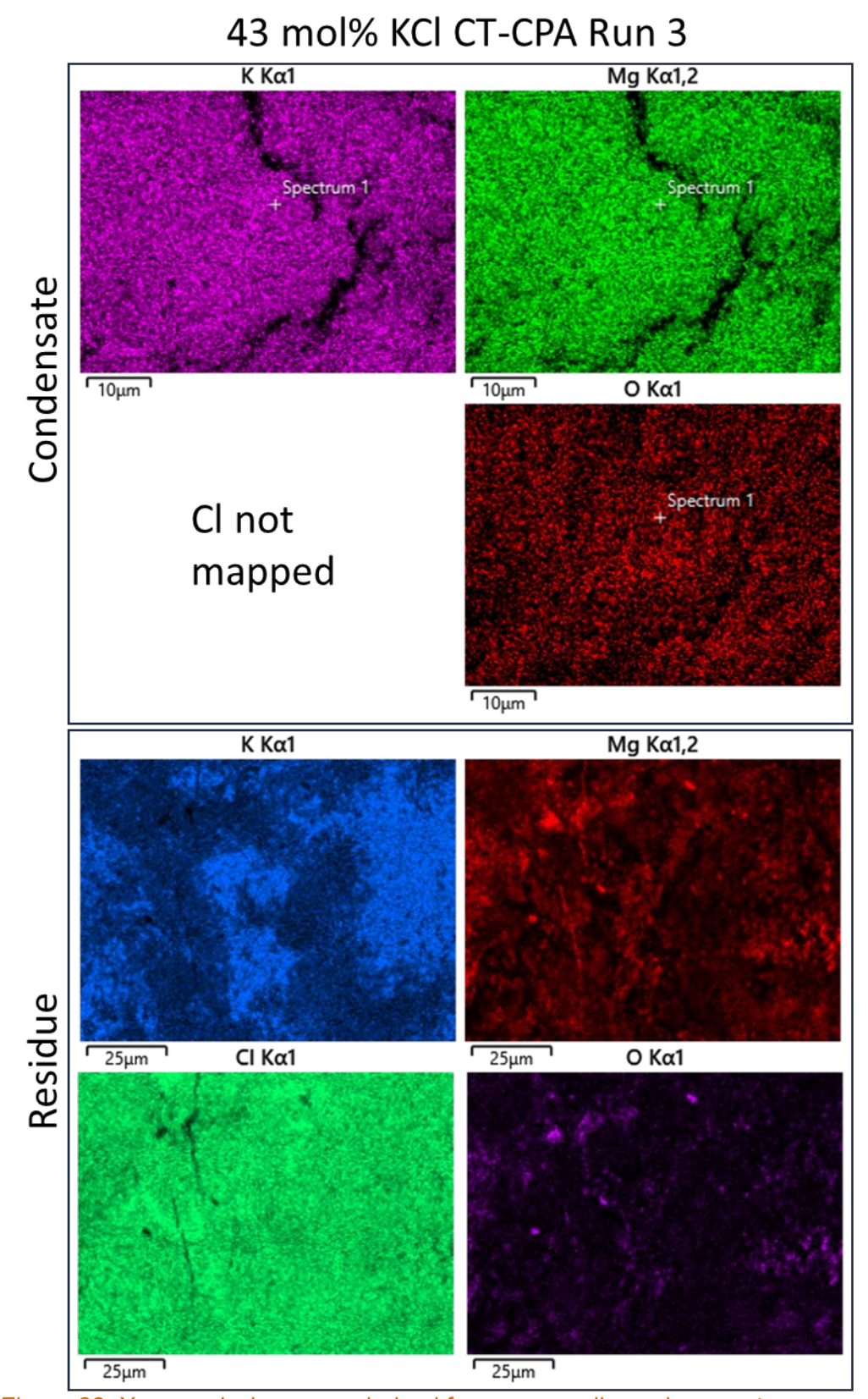


Figure 22. X-ray emission maps derived from energy dispersive spectroscopy.

Condensed solids from the 65 mol% starting composition can be seen in Figure 23. At lower magnifications two main morphologies are present, a diffuse structureless portion and a fraction that forms clusters. At higher magnifications, both morphologies are dominated by grains of homogenous size and two predominant morphologies. As in the 43 mol% KCl sample, the 65 mol% sample shows subhedral to euhedral grains approximately 0.5 to 1  $\mu$ m in diameter. In addition, a significant number of particles display a spherical morphology of marginally larger diameter. The residue fraction is similar to that of the 43 mol% KCl sample. Here, it appears blocky at lower magnifications but at higher magnifications interconnected hexagonal crystals are observed.

# 

Figure 23. Secondary electron images of the condensate and reside fractions for the 65 mol% KCl mixture.

The distribution of K and Mg in the condensate fraction is homogenous (Fig. 24). In the residue fraction it appears there is a strong spatial correlation with Mg and O, again suggesting a discrete MgO phase, similar to the 43 mol% KCl sample. Also, there appears to be a spatial anticorrelation with the distribution of Cl and O, specifically with the Cl-rich zones correlating to regions of high K content. This is consistent with the XRD results where a discrete KCl phase is identified

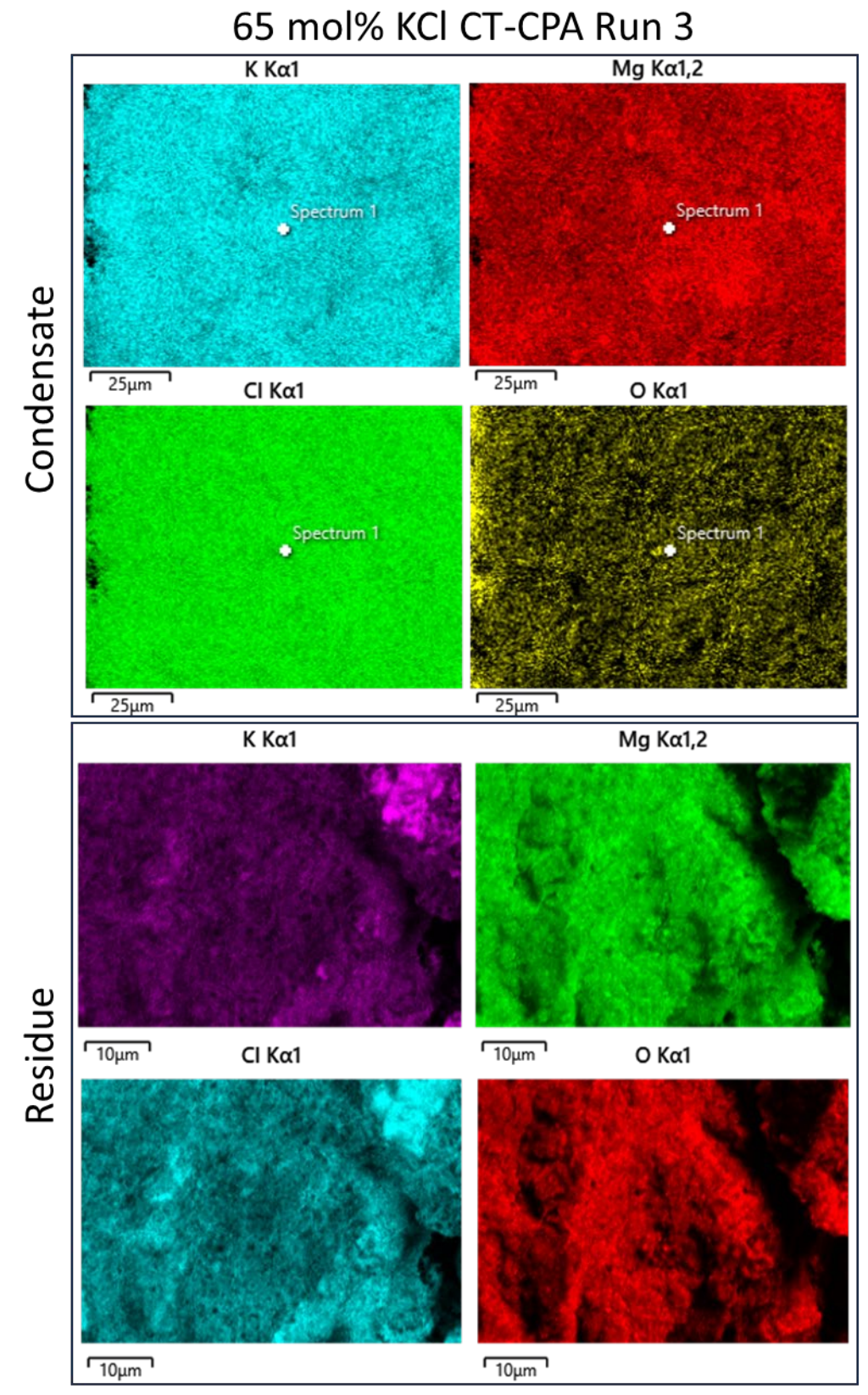


Figure 24. X-ray emission maps derived from energy dispersive spectroscopy.

The 69 mol% KCl sample appears to be the most homogenous with respect to grain size and morphology (Fig. 25). At high magnification, the grain size and morphology are similar to those from the previous two compositions for the condensate fraction. Unlike the previous two compositions, the residue fraction here displays a much finer grain size, with no discernable morphology present, even at higher magnifications.

## 

### 69 mol% KCl CT-CPA Run 3

Figure 25. Secondary electron images of the condensate and residue fractions for the 69 mol % KCl mixture.

The spatial distribution of K and Mg can be seen in Figure 26. What appears to be unique in this sample is the homogenous spatial distribution of Cl in both the condensate and residue fractions and its spatial association with K and Mg. From these data alone it is not feasible to speculate as to the phase association, but if the XRD data are considered, it is likely both fractions contain a pure KCl phase mixed with a KMgCl<sub>3</sub> phase (carnallite). In additional SEM-EDS maps produced (not shown here), it was observed that a pure KCl phase with similar grain morphology as seen in Figure 25 was evident. However, unlike other compositions, there appeared to be an amorphous glass-like phase cementing individual grains together. The residue fraction does contain similarities to previous samples, that is in the spatial association of Mg and O.

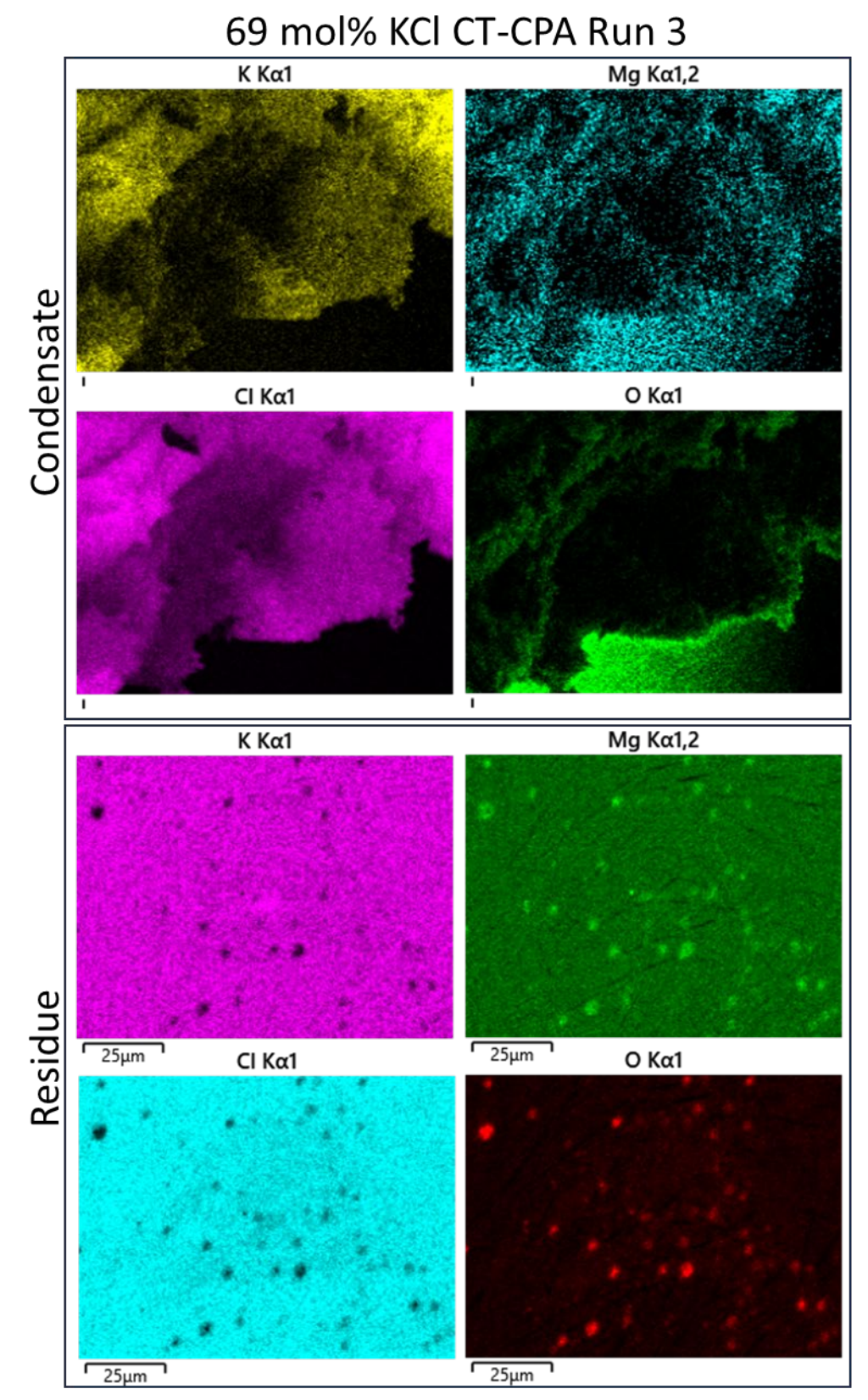


Figure 26. X-ray emission maps derived from energy dispersive spectroscopy.

The 69 mol% KCl eutectic mixture was doped with 300 ppm by weight with Fe, Ni, and Cr. These elements represent potential containment material contaminants within molten salt reactors. This salt was tested for its volatility similar to the compositions previously summarized. Our goal was to determine if these impurities have an affinity for the vapor or melt phase. Images of the condensate and residue fractions can be observed in Figure 27. The grain size and morphology of the condensate are generally unremarkable and similar to those previously described. The residue fraction however displays unique grain morphologies not observed in any other pure composition. For example, several grains display radial growth that forms quasispherical grain clusters. In the bottom right part of the bottom right inset SEM image, one will observe dipyramidal tetrahedron. These were also observed in one run of pure 69 mol% KCl and will be discussed below.

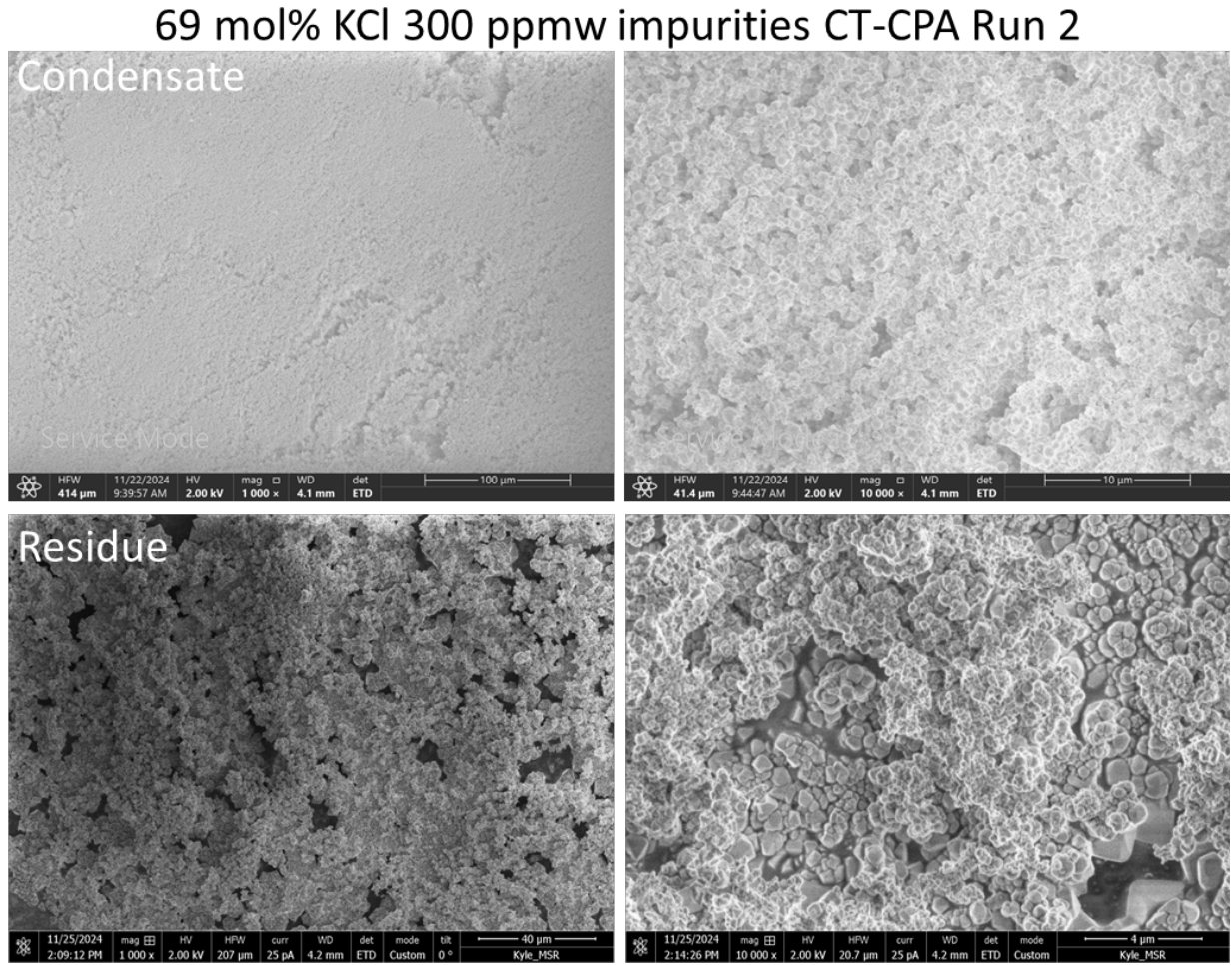


Figure 27. Secondary electron images of condensate and residue fractions for the 69 mol % KCl mixture doped with 300 ppm by weight Fe, Cr, and Ni.

The distribution of K and Mg can be seen in Figure 28. For the condensate fraction, both K and Mg are homogenously distributed and have a strong correlation to the distribution of Cl. The association of Mg and O in the residue phase is the strongest amongst any of the previously described samples. This correlates well with the observed XRD data in Figure 20. Given these results and that from XRD, two hypotheses have been proposed for the presence of oxygen in the system: 1) the oxygen is derived from the presence of impurity oxides in the starting FeCl<sub>2</sub>, NiCl<sub>2</sub>, or CrCl<sub>2</sub> and 2) the rate of oxidation from MgCl<sub>2</sub> to MgO is extremely fast and kinetically

favorable, thus the conversion to oxide is a post-experiment phenomenon and is not related to oxygen contamination from either the impurity salts or from the experiment itself. Future work will focus on determining which of these is dominant and how to best address it.

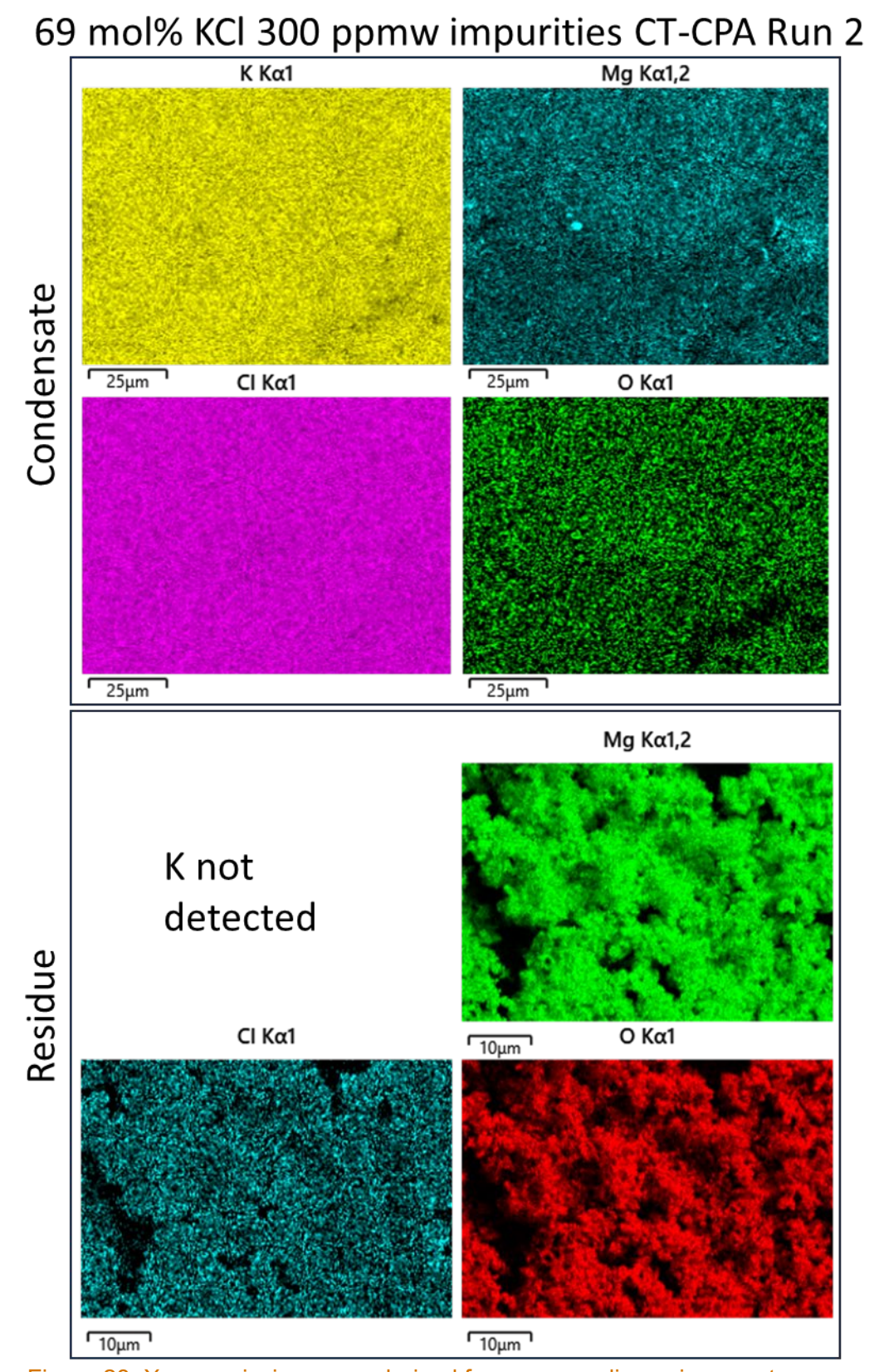


Figure 28. X-ray emission maps derived from energy dispersive spectroscopy.

Characterization of the condensate and residue fractions via XRD and SEM-EDS reveals that in almost all experiments, the condensate fraction is homogenous from both a crystalline phase and chemical perspective. The residue fraction is evidently more complex and typically contains phases detrimental to both bench-scale laboratory thermophysical property measurements and more generally, to molten salt reactor operation as a whole. These two techniques were used to provide a general sense of the nature of volatility of the KCl-MgCl<sub>2</sub> system at three eutectic compositions. They provided evidence of the phases present and the spatial distribution of the main components in the condensate and residue fractions.

An additional analytical technique was needed to assess the congruity of volatilization in the KCl-MgCl<sub>2</sub> system. Here, LIBS was chosen because of its relatively simple implementation, access, and in-team expertise. As implemented to the volatility results, it should be noted that currently, this is purely a semi-quantitative approach. Additional method development, namely the calibration using certified reference materials, is needed to produce truly quantitative data.

A calibration curve was developed to determine the mol% KCl content of each condensate and residue fraction. Initially, the same calibration curve shown in Fig. 4 was used; however, unreasonable mol% KCl values were produced. Upon further consideration, it was noted that in the early EGA-MS experiments, Cl was the only evolved gas detected from all salt mixtures tested (Fig. 12), evidence of open system behavior. Furthermore, SEM-EDS results for most residue and condensate fractions show that conversion from MgCl<sub>2</sub> to MgO is likely. For these data, it is assumed this conversion occurred post experiment and is not related to oxygen contamination from the salts or the experiment itself. Thus, normalizing the K and Mg intensities to Cl intensities is problematic and does not represent the true K/Cl or Mg/Cl peak ratios. To combat this, K peak intensities were normalized to Mg peak intensities using the same data used to make Fig. 4. The resulting calibration curve is shown below in Figure 29. The relationship between K/Mg ratio and mol% KCl is exponential and the equation defining the calibration curve is reflected as such. A strong Pearson's correlation coefficient of 0.9978 is produced using this relationship.

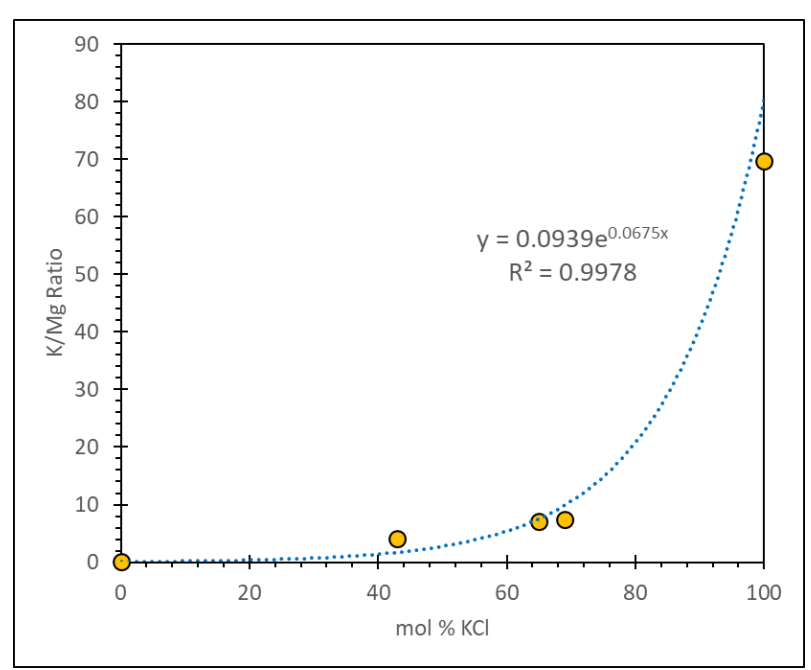


Figure 29. Calibration curve used to determine mol% KCl content for the condensate and residue fractions from LIBS spectral data.

Each composition was analyzed in triplicate to best assess the reproducibility of the CT-EGA method. Mass balance calculations were performed using the determined mol% KCl content derived by LIBS. In most cases, mass balance is preserved within 10% between known starting mass fraction and end products of the condensate and residue fractions.

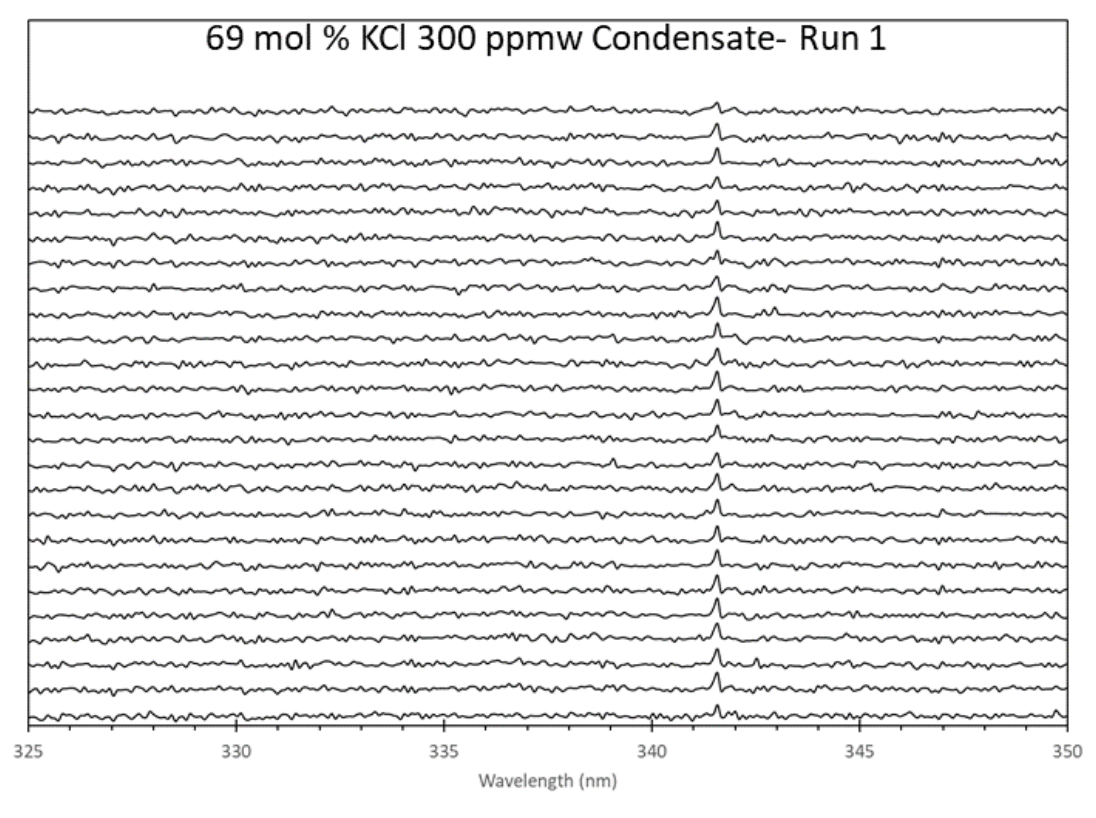
Each composition displays incongruent volatilization. The magnitude of incongruity appears to loosely scale with deviation from a 50/50 mixture (Table 5). For example, the 43 mol% KCl mixture displays the closest congruent volatilization whereas the 69 mol% KCl mixture is on average 17% different than the starting composition. These data suggest the vapors emanating from the molten salt are enriched in KCl relative to MgCl<sub>2</sub>, implying the composition of the melt evolves towards enrichment of MgCl<sub>2</sub>. This may have significant impacts on the efficacy of the KCl-MgCl<sub>2</sub> system for use in MSRs. However, given the novelty of this approach, additional work is needed to verify the trends established herein.

Elemental data were also collected using LIBS to assess how the incorporation of surrogate corrosion products Fe, Ni, and Cr affect or behave in the KCl-MgCl<sub>2</sub> system. Both the condensate and residue fractions were analyzed. Consistently only Ni was observed in the condensate fraction (Fig. 30). Iron and Cr were identified in several locations within the residue but in random spatial distribution, suggesting diffusion of these elements is relatively slow in molten KCl-MgCl<sub>2</sub>. Generally, the concentration of impurities in molten salts is expected to increase due to the in-growth of corrosion products (Hartman and Paviet, 2022). The LIBS data suggests these impurities are not removed from the system via volatility, a positive occurrence of which may have been an unintended benefit as it would have worked to naturally purify the salts via a process similar to distillation. Instead, the increase in concentration of corrosionproduct impurities must be taken into account during reactor operation. Depending on the diffusion rate of these impurities, they may coalesce into zones and cause local perturbations in thermal, density, or viscosity characteristics of the molten salt, Furthermore, it is reasonable to postulate a scenario where the concentration of these impurities reaches a solubility limit causing their precipitation from the melt. Either of these scenarios may have significant unintended consequences for reactor operation.

Table 5. Results of LIBS spectral analysis for condensate and residue fractions for all eutectic compositions tested.

Sample	K/Mg	sd	mol% KCl
43 mol % KCl t1 Condensate	1.80	0.39	43.77
43 mol % KCl t1 Residue	1.64	0.46	42.40
43 mol % KCl t3 Condensate	1.99	0.39	45.22
43 mol % KCl t3 Residue	1.99	0.44	45.23
43 mol % KCl t4 Condensate	3.63	1.10	54.13

65 mol % KCl t1 Condensate	10.29	1.39	69.59
65 mol % KCl t1 Residue	2.20	0.25	46.76
65 mol % KCl t2 Condensate	3.20	0.34	52.26
65 mol % KCl t2 Residue	2.76	0.31	50.10
65 mol % KCl_t3 Condensate	2.41	0.35	48.05
65 mol % KCI_t3 Residue	1.84	0.60	44.11
69 mol % KCl t2 Condensate	3.78	0.42	54.76
69 mol % KCl t2 Residue	1.08	0.31	36.18
69 mol % KCl t3 Condensate	2.60	0.52	49.17
69 mol % KCl t3 Residue	1.95	0.27	44.96
69 mol % KCl t4 Condensate	3.59	0.91	53.99
69 mol % KCl t4 Residue	0.19	0.07	10.35
69 mol % KCl trace impurities t1 Condensate	4.41	0.75	57.02
69 mol % KCI trace impurities t1 Residue	0.22	0.14	12.50
69 mol % KCI trace impurities t2 Condensate	6.52	0.92	62.81
69 mol % KCI trace impurities t2 Residue	0.19	0.07	10.70



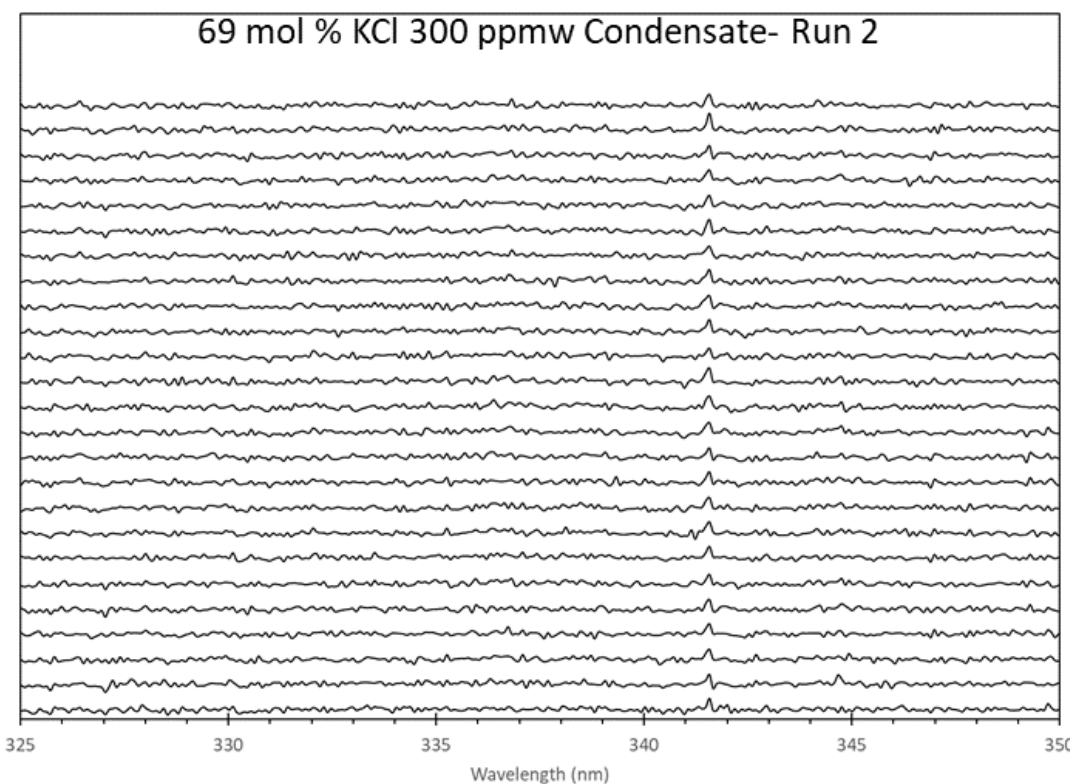


Figure 30. Plots of LIBS emission spectrum from 325 to 350 nm. Note small peak at 341.5 nm, resulting from the presence of Ni in the condensate fraction. Nickel was the only doped impurity identified in the condensate fraction.

### 4.0 Conclusion

Select thermophysical properties were measured on the KCl-MgCl<sub>2</sub> salt system in the temperature range of 500-800 °C. Several properties were investigated, including specific enthalpy, heat capacity, density, and volatility. Below a few key points are presented based on the results of work performed in FY24.

A significant amount of time was spent developing an improved sample handling protocol and sample preparation methodology. Although most chloride salts are hygroscopic and sensitive to oxygen contamination, some are more prone to contamination than others. It was discovered early in this endeavor that MgCl<sub>2</sub> is especially problematic. This salt is extremely sensitive to oxygen and water contamination and if present, will convert stoichiometrically to MgO when heated. Thus, great care must be exercised when working with this salt. To that end, a method of careful storage, sample transport, and analysis were developed to mitigate these effects. Prior to thermophysical property testing, all samples were characterized for baseline water and elemental trace impurity contents. A more robust method was developed to prepare samples for thermophysical property analysis, with emphasis placed on the ability to aliquot representative subsamples from mixed end member compositions. Any thermophysical property derived by experiment is directly tied to the confidence of the purity and composition of the material being tested; therefore, with a more robust protocol in place, it is believed the quality of the data produced is elevated relative to previous work.

Measurements were performed on both pure salt mixtures and mixtures containing trace impurities. The eutectic compositions of 43, 65, and 69 mol % KCl were spiked with 1 wt% water and 300 and 600 ppm Fe, Ni, and Cr. The concentrations at which these salts were spiked with corrosion product surrogates were designed to simulate estimates of the ingrowth of corrosion products at reactor conditions over the period of ~3.5 years (Hartman and Paviet, 2022). The results presented here suggest there is minimal effect on the specific enthalpy or heat capacity of the KCI-MgCl<sub>2</sub> system, at least at the levels of contamination tested. Simple hypothesis testing between the two datasets show no significant statistical difference between the two. Currently, it is not known if this is a true characteristic or is masked by errors associated with the measurement. On the former, it is envisioned these results may be due to the relatively small samples used for testing via drop calorimetry. That is, only approximately 20 mg of sample is used for these experiments, thus only micrograms of contaminant are added; therefore, it may be a case that this small amount of material does not produce a change in signal measurable by the instrument. If greater masses of sample were used, which would require proportionately higher masses of contaminant to be added (to maintain a concentration of 300 or 600 ppm), then perhaps this would produce a signal resolvable by the drop calorimeter. Future work is aimed at addressing these issues.

Corrosion of (pure) Ni containment vessels used in drop calorimetry was amplified for samples containing elevated water contents and corrosion product surrogates. As described above, the crucibles used for this work are hermetically sealed using a laser welder. There was an estimated 40% failure rate of these welds from these specific samples, which is approximately 35% higher than the typical failure rate of the pure components. Although this was purely a nuisance for the work performed here as it dramatically increased the time to produce meaningful data, the occurrence of it suggests further investigation into the corrosion itself is warranted.

Development of a method to measure density is still ongoing at PNNL. Preliminary results from thermomechanical analysis show promise of a viable method (see Fig. 11 and associated

Conclusion 48

discussion). However, further development of this method is needed. Chiefly, future work will be directed at salt containment during analysis.

Assessing volatility of molten salt by directs means has proved to be challenging. Early attempts this year using EGA coupled with mass spectrometry resulted in limited utility. The main challenge is finding a way to keep the volatilized material in the vapor phase upon transport to the back-end analytical instrument. Given the high eutectic melting temperature of the KCl-MgCl<sub>2</sub> salt system, and many others like it, this technique is not viable without further development and fabrication of custom components.

An indirect method to assess volatility has been developed. Here, a conductively cooled cold trap is placed in close proximity to the sample at melt conditions. As the sample volatilizes, the vapor migrates to the cold trap where it then condenses. Tests conducted using this methodology proved remarkably successful, albeit conducted under a limited set of conditions. All samples were tested at the same temperature and were held at that temperature for an identical length of time. In nearly all cases, characterization of the condensed vapor resulted in a composition different from that of the starting material. This incongruent volatilization behavior may have profound impacts as it implies the composition of the melt changes over time. If the composition evolves, then so do its thermophysical properties like heat capacity, density, and viscosity. This evolved composition will likely have other characteristics that differ from its parent material, e.g., corrosivity, rates of diffusion of actinide species and contaminants. Clearly, understanding the magnitude of incongruent volatilization should be of paramount importance for any planned fuel or coolant salt system. Future work in this area is planned and includes assessing how compositions evolve over time and temperature.

Conclusion 49

### 5.0 References

- Abdel-Aal, H.K. Magnesium: From Resources to Production. CRC Press, 2018.
- Anderson, N., Sabharwall, P. 2012. Molten salt mixture properties (KF-ZrF4 and KCl-MgCl2) for use in RELAP5-3D for high-temperature reactor application. *Nuclear technology* 178(3), 3350340.
- Baumli, P., Kaptay, G. 2008. Wettability of carbon surfaces by pure molten alkali chlorides and their penetration into a porous graphite substrate. *Materials Science and Engineering*. v. 495. no. 1. p. 192-196.
- Berns, J., Lacovic, R. 1968. Capillary rise in the annular region of concentric cylinders during coast periods of Atlas Centaur flights. *National Aeronautics and Space Administration Technical Memorandum TM X-1558*. 13 pp.
- Betzler, B. R., F. Heidet, B. Feng, C. Rabiti, T. Sofu, and N. R. Brown. 2019. Modeling and simulation functional needs for molten salt reactor licensing. *Nuclear Engineering and Design* 355. <a href="https://doi.org/ARTN 110308">https://doi.org/ARTN 110308</a>.
- Briggs, R., 1964. Molten-Salt Reactor Program- Semiannual progress report for period ending January 31, 1964. *Oak Ridge National Laboratory ORNL-3708*.
- Culkin, F., Cox, R. 1966. Sodium, potassium, magnesium, calcium, and strontium in sea water. In *Deep Sea Research and Oceanographic Abstracts*. Elsevier. v. 13, p. 789-804.
- Hartman, T., Paviet, P. 2022. Corrosion of containment alloys in molten salt reactors and the prospect of online monitoring. *Journal of Nuclear Fuel Cycle*. v. 20. no. 1. p. 43-63. DOI: 10.7733/jnfcwt.2022.005.
- Johannes, W., Holtz, F. 1996. Properties of hydrous haplogranitic melts. *In* Petrogenesis and Experimental Petrology of Granitic Rocks. *Minerals and Rocks*. v. 22. Springer, Berlin, Heidelberg. DOI: 10.1007/978-3-642-61049-3\_3.
- Lonergan, J., Goncharov, V., Swinhart, M., Makovsky, K., Rollog, M., McNamara, B., Clark, R., Cutforth, D., Armstrong, C., Guo, X., Paviet, P. 2023. Thermodynamic investigation of the NaCl-KCl salt system from 25 to 950 °C. *Journal of Molecular Liquids*. v. 391. part A. DOI: 10.1016/j.molliq.2023.122591.
- Li, Y., Xu, X., Wang, X., Li, P., Hao, Q., Xiao, B. 2017. Survey and evaluation of equations for thermophysical properties of binary/ternary eutectic salts from NaCl, KCl, MgCl<sub>2</sub>, CaCl<sub>2</sub>, ZnCl<sub>2</sub> for heat transfer and thermal storage fluids in CSP. *Solar Energy*. v. 152. p. 57-79.
- Li, X., Liu, W., Tang, Z., Xu, T., Wang, J. 2020. Insight into dynamic interaction of molten MgCl<sub>2</sub>-NaCl-KCl with impurity water via FPMD simulations. *Journal of Molecular Liquids*. v. 314. DOI: 10.1016/j.molliq.2020.113596.
- Lu, J., Yang, S., Rong, Z., Pan, G., Ding, J., Liu, S., Wei, X., Wang, W. 2021. Thermal properties of KCl-MgCl<sub>2</sub> eutectic salt for high-temperature heat transfer and thermal storage system. *Solar Energy Materials and Solar Cells*. v. 228. DOI: 10.1016/j.solmat.2021.111130.
- Morel, C. 1970. Surface tensions of molten salts and contact angle measurements of molten salts on solids. *Commission of the European Communities EUR-4482*. v. 2. no. 6.

References 50

- NIST WebBook. NIST Standard Reference Database Number 69. Linstrom, P., Mallard, W eds. National Institute of Standards and Technology, Gaithersburg, MD, 20899. DOI: 10.18434/T4D303. Retrieved December 17, 2024.
- Noorie, Kalkhoran, O., Litskevich, D., Detkina, A., Jain, L., Carland-Glover, G., Merk, B. 2022. On the employment of a chloride or fluoride salt fuel system in Advanced Molten Salt Reactors, Part 1: Thermophysical Properties and Core Criticality. *Energies*. v. 15.
- Perry, G., Fletcher, H. 1992. The magnesium chloride-potassium chloride phase diagram. *Journal of Phase Equilibria*. v. 14. no. 2.
- PNNL-35354. Harris, M., Makovsky, K., Lonergan, J. 2023. Towards robust thermophysical property measurements at Pacific Northwest National Laboratory.
- Raiman, S., Lee, S. 2018. Aggregation and data analysis of corrosion studies in molten chloride and fluoride salts. *Journal of Nuclear Materials*. v. 511. p. 523-535.
- Williams, D. 2006. Assessment of candidate molten salt coolants for the NGNP/NHI Heat Transfer Loop. *ORNL/TM-2006/69*. 44 pp.
- Xiao, Y., Tang, K. 2009. Solubility of alumina in molten chloride-fluoride melts. *In Proceedings of the VIII International Conference on molten slags, fluxes, and salts.*
- Xu, X., Wang, X., Li, P., Li, Y., Hao, Q., Xiao, B., Elsentriecy, H., Gervasio, D. 2018. Experimental test properties of KCl-MgCl<sub>2</sub> eutectic molten salt for heat transfer and thermal storage fluid in concentrated solar power systems. *Journal of Solar Energy Engineering*. v. 140.

References 51

## Appendix A – Thermomechanical Analysis Sample Container Design

### 1.0 Background

PNNL currently uses a TMA commercially produced by Netzsch (TMA 402 F1 Hyperion). This instrument is configured with an alumina support tube and pushrod that limits the sample container to less than 10 mm diameter and 30 mm length dimensionally and thermally limited to temperatures less than 1550°C. Generally, this instrument is used on solid samples; however, Netzsch supplies sample containers for special applications such as powders, pastes, and liquids. The containers available in Netzsch's online catalog only contain Al<sub>2</sub>O<sub>3</sub>, fused silica, sapphire, and graphite. The instrument measures the volume dependence on the temperature of materials by applying a modest force (minimum 1 mN) to a sample or sample container with a dilatometer. Special sample containers are designed to have a cylindrical cup, the crucible, that contains the sample with a plunger situated so it rests on the top horizontal liquid surface. The plunger moves up and down in reference to the crucible bottom upon a change in the volume of the liquid sample. This change in plunger height is measured and the sample material volume dependence on temperature can be calculated.

The most significant challenge currently facing TMA measurement is liquid salt leakage from the sample container during measurement, resulting in no useful liquid sample volume data being generated. Figure 31 illustrates typical salt leakage from a sample container. The salt leaks from the annular region between the plunger and the crucible wall. Various attempts have been made to prevent leakage, including decreasing the annular gap from the Netzsch crucible design to 0.0335 mm in our in-house Al2O3 crucible design. However, both the Netzsch fused silica and Al2O3 crucibles experienced leakage. An in-house crucible made of boron nitride (BN) also leaked, but this crucible suffered from a cracked wall, indicating that the cause of the leak may differ from that observed with the Al2O3 and fused silica materials.

The sample containers consistently leak from the annular region (except for the BN sample container). This region of flow is governed by gravitational force, including hydrostatic force and buoyancy force, the force applied by the instrument (necessary for measurement), and, importantly, the surface tension force. The gravitational forces are well covered by numerous texts, the instrument force is recorded with high precision and accuracy, and the surface tension force in an annular region has been documented in the literature (Berns and Lacovic, 1968). Given that the different sample container designs have a consistent mode of failure and that the static forces on this region have been well developed in the literature, a new sample container should be designed with molten salt properties and interactions factored into the regional flow behavior to prevent annular leakage.

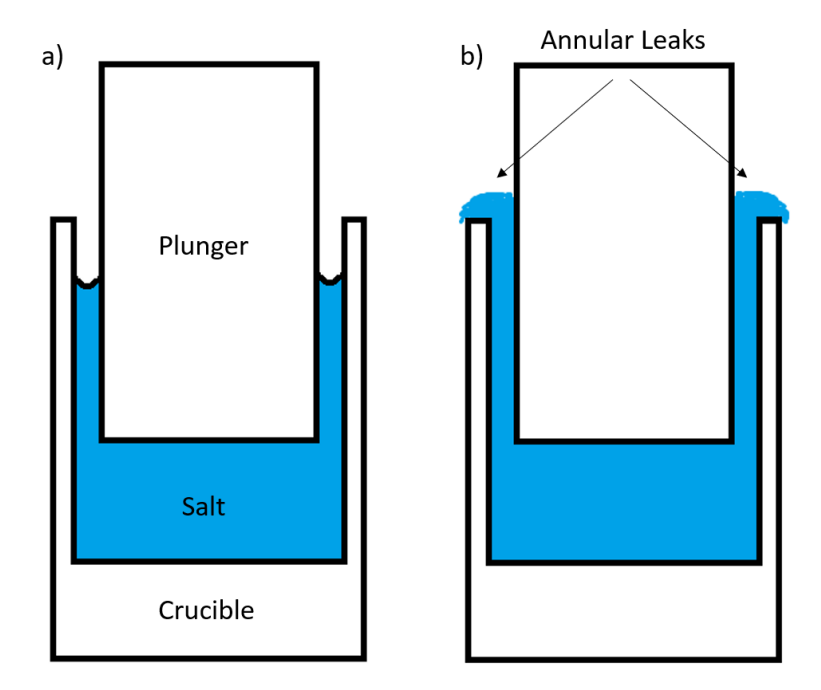


Figure 31. Two cross-sections of a typical TMA crucible (white) containing salt (blue) at two different times. a.) Just after melt. b.) Sometime between melt and the end of the measurement, salt leaks from the annular region between the plunger and the crucible wall.

### 2.0 Theory

The equilibrium position of capillary rise in an annular region is a function of the pressures exerted on the fluid. Some pressures are created by gravitational forces on the fluid and plunger, namely, the hydrostatic pressure of the fluid head in the annulus,  $P_{gB}$ , the displacement of fluid by the plunger into the annulus,  $P_{gA}$ , and the pressure caused by the weight of the plunger,  $P_p$ . The surface tension pressure on the plunger and fluid in the annulus,  $P_{\sigma A}$  and  $P_{\sigma B}$ , respectively, is the result of the curved salt/cover-gas interface in the annular region. The instrument also exerts a force on the sample container to receive feedback on a change in the length of the sample. This force is applied to the top of the plunger and bottom of the crucible,  $P_n$ , by the instrument continuously throughout the measurement to maintain contact between the instrument and sample for an accurate sample length measurement. Figure 32 shows the pressure diagram.

In the pressure diagram, Figure 32, points A and B are at the same pressure because they are at the same fluid level according to Pascal's Principle for fluids at mechanical equilibrium. At point A the total pressure on the liquid surface is the sum of the force from the plunger,  $P_p$ , ambient pressure,  $P_{amb}$ , instrument pressure,  $P_n$ , surface tension,  $P_{\sigma A}$ , and liquid sample displacement,  $P_{qA}$ , equation (1).

$$P_{A} = P_{amb} + P_{p} + P_{n} - P_{aA} - P_{\sigma A} \tag{1}$$

 $P_{amb}$ ,  $P_p$ ,  $P_n$ , are taken to be positive because they act in the downward direction on the liquid surface while the surface tension pressure,  $P_{\sigma A}$ , and fluid displacement (buoyancy pressure),  $P_{gA}$ , are negative because they act in the opposite direction. The surface tension force points in the upward direction, away from the fluid surface only when the contact angle (CA),  $\theta$ , is greater than 90° (non-wetting). Under this condition, the liquid is driven down because the cohesion force on the liquid is greater than the adhesion force between the liquid and the container material. The net result is the surface tension creates a force that drives the plunger away from the liquid and drives the surface of the liquid in the annulus down out of the annular region.

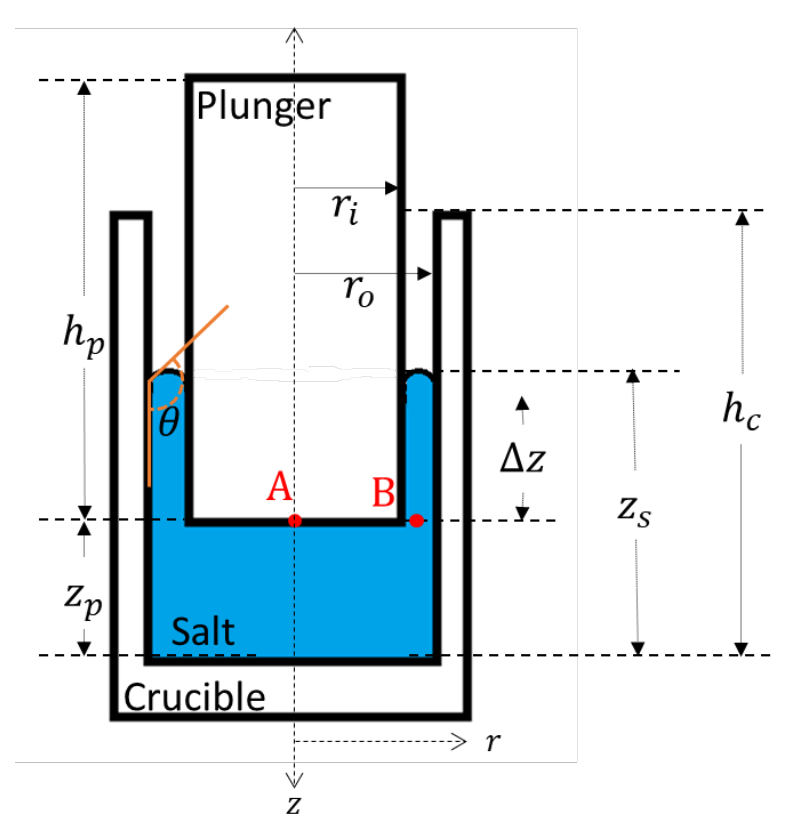


Figure 32. Pressure diagram for the TM sample container system.

At point *B* the total pressure is the sum of the ambient pressure,  $P_{amb.}$ , hydrostatic pressure,  $P_{qB}$ , and surface tension pressure in the annulus,  $P_{\sigma B}$ , equation (2).

$$P_B = P_{amb.} + P_{gB} + P_{\sigma B} \tag{2}$$

The same convention is taken here where downward pressures pointing toward the liquid surface, are positive. We can set equation (1) equal to equation (2) and eliminate the ambient pressure, equation (3).

$$P_p + P_n - P_{gA} - P_{\sigma A} = P_{gB} + P_{\sigma B} \tag{3}$$

Each pressure in equation (3) can be put in terms of the crucible dimensions, material properties, and external forces. Equations (4.a-f) define the pressure terms and equation (4.g) substitutes the pressure values into equation (3).

$$P_p = \rho_p hg \tag{4.a}$$

$$P_n = \frac{F_n}{\pi r_i^2} \tag{4.b}$$

$$P_{gA} = \frac{\rho_s V_a g}{\pi r_i^2} = \frac{\rho_s \Delta z (r_o^2 - r_i^2) g}{r_i^2}$$
(4.c)

$$P_{\sigma A} = -\frac{2\sigma\cos(\theta)}{r_i} \tag{4.d}$$

$$P_{gB} = \frac{\rho_s V_a g}{\pi (r_o^2 - r_i^2)} = \rho_s \Delta z g \tag{4.e}$$

$$P_{\sigma A} = -\frac{2\sigma\cos(\theta)}{r_o - r_i} \tag{4.f}$$

$$\rho_p h_p g + \frac{F_n}{\pi r_i^2} - \frac{\rho_s \Delta z (r_o^2 - r_i^2) g}{r_i^2} + \frac{2\sigma \cos(\theta)}{r_i} = \rho_s \Delta z g - \frac{2\sigma \cos(\theta)}{r_o - r_i}$$

$$\tag{4.g}$$

 $\rho_p$  is the density of the plunger material,  $h_p$  is the height of the plunger, g is the acceleration due to gravity,  $F_n$  is the force supplied by the TMA instrument,  $r_i$  is the radius of the plunger,  $\rho_s$  is the density of the salt,  $\Delta z$  is the vertical distance from the bottom of the plunger to the salt/cover-gas interface in the annulus,  $r_o$  is the inner radius of the crucible,  $\sigma$  is the surface tension of the salt, and  $\theta$  is the contact angle between the salt and the plunger/crucible wall (assuming they are the same).

A leak occurs when the equilibrium position of the salt/cover-gas interface is higher than the wall of the crucible,  $h_c$ . The distance,  $\Delta z$ , gives the position of the interface relative to the bottom of the plunger. Since the plunger does not have a fixed vertical position relative to the crucible,  $\Delta z$  is not easily determined. The position of the plunger is a function of the sample size and the total amount of sample in the annulus. Since the position of the plunger is a function of the sample volume and the sample volume can change significantly due to sample size variation and thermal expansion during a measurement, a leak cannot be determined simply by comparing  $\Delta z$  to  $h_c$  for all values of  $\Delta z$ . However, assuming the total sample volume does not exceed the crucible reservoir volume, a value of  $\Delta z$  which is less than or equal to 0 is a non-leak position. Conversely, a  $\Delta z$  greater than  $h_c$  is a leak position. Therefore, it is useful to solve equation (4.g) in terms of  $\Delta z$  as seen in equation (5).

$$\Delta z = \frac{\rho_p h_p}{\rho_s \kappa^2} + \frac{F_n}{\rho_s g \pi r_o^2} + \frac{2\sigma \cos(\theta)}{\Delta r \rho_s g \kappa}$$
Where
$$\kappa = \frac{r_o}{r_i} \text{ and } \Delta r = (r_o - r_i)$$
(5)

The first two terms on the right-hand-side of equation (5) are necessarily positive and only positively increase the value of  $\Delta z$ . The surface tension force, represented by the third term on the right-hand-side of equation (5), is positive for wetting contact angles and negative for non-wetting contact angles. This derivation assumed the surface tension acted opposite to  $P_p$  and  $P_n$ , however, the equation is still valid for wetting contact angles so long as the density of the plunger is less than the density of the salt and the salt is not in a leak position.

A leak position can be determined if the sample volume is known by using equation (6).

$$V_{S} = \Delta z \pi \left(r_{o}^{2} - r_{i}^{2}\right) + z_{p} \pi r_{o}^{2}$$

$$\frac{V_{S}}{\pi r_{o}^{2}} = \frac{\Delta z \left(r_{o}^{2} - r_{i}^{2}\right)}{r_{o}^{2}} + \left(z_{p} - z_{S} + z_{S}\right)$$

$$\frac{V_{S}}{\pi r_{o}^{2}} = \Delta z - \frac{\Delta z}{\kappa^{2}} + (\Delta z + z_{S})$$

$$z_{S} = \frac{V_{S}}{\pi r_{o}^{2}} + \Delta z \left(\frac{1}{\kappa^{2}} - 2\right)$$
(6)

 $V_S$  is the total salt volume,  $z_p$  is the distance from the inner bottom of the crucible to the bottom of the plunger, and  $z_S$  is the distance from the inner bottom of the crucible to the liquid peak height in the annulus. If  $z_S$  is greater than  $h_c$  then the salt has reached a leak position.

Equations (5) and (6) make up the physical model of the sample container system. The model is valid for  $\theta < 90^{\circ}$ ,  $\rho_s > \rho_p$  and  $z_s < (h_c \text{ and } h_p)$  and for  $\theta > 90^{\circ}$ ,  $z_s < (h_c \text{ and } h_p)$ .

### 3.0 Sample Container Design

### 3.1 **Bounding Conditions**

This section covers the boundary conditions of the sample container design such as the compatibility of the sample container material with molten salt at high temperatures and support a non-wetting CA. Additionally, the sample container must be robust, reusable, inexpensive, fit within the TMA testing components, and easily machinable. The requirements of the method are then compared to available materials. As each material property requirement is discussed, the viability of certain materials will be ruled out, at which point the material properties will no longer be included in the discussion.

Molten salts are highly corrosive, require high temperatures, and wet most materials. Additionally, molten salt is a broad category of ionic substance with a wide range of material properties that no single sample container design fits. Therefore, the boundaries given for this problem are specifically related to our current work with KCl and MgCl<sub>2</sub> and their mixtures. The boundary conditions will be different for other chemical compositions.

### 3.1.1 Temperature Limits

The temperature limits of KCl and MgCl<sub>2</sub> are related to their boiling point, 1420°C and 1412°C, respectively, and within the TMA machine limit, 1550°C. However, the vapor pressure of these salts (Williams, 2006) is high enough to significantly shift sample mass and form vapor deposits over the measurement period at temperatures close to their pure component melting points, 770°C and 714°C, respectively. Therefore, to reduce the amount of vapor produced by these salts and their mixtures the temperature limit is set to 850°C. The sample container material should be compatible with temperatures up to 850°C.

### 3.1.2 Chemical Compatibility

The sample container material must be chemically compatible with the molten salt. KCl and MgCl<sub>2</sub> are corrosive and can react with a multitude of steel compositions (Williams, 2006). Chloride salts also have a higher corrosion rate with nickel alloys than fluoride salts (Williams, 2006). Chloride salts can react with noble metals as in aqueous mixtures containing high concentrations of hydrochloric acid. Ceramics such as graphite, boron nitride, quartz. and alumina are chemically compatible with chloride salts (Baumli and Kaptay, 2008; Xiao and Tang, 2009; Raiman and Lee, 2018).

### 3.1.3 Contact Angle

There is little data on the contact angle (CA) of molten salts on compatible materials. Some data exist for graphite and platinum (Morel, 1970; Baumli and Kaptay, 2008). Graphite supported a higher CA when pretreated by degassing (Morel, 1970). CAs increase as the purity of the salt increases (Morel, 1970). Oak Ridge (1964) measured a CA of 68° on graphite for KCl, and measured a CA of ~35° on Nickel for NaCl-KCl mixture (Briggs, 1964). The CA data for Li<sub>2</sub>BeF<sub>4</sub> indicates that CAs should decrease on metal surfaces in the following order: Au, Pt, Ni, and Cu. In the instance of Li<sub>2</sub>BeF<sub>4</sub>, each CA decreases by about 10-20° for each substance. Assuming the same trend for our salt of interest and a similar low contact angle for Ni as seen with the NaCl-KCl mixture, the contact angle on Au and Pt will also be wetting for the salts of interest.

Lonergan et al. (2023) used boron nitride (BN) crucibles in a TMA instrument with instrument forces up to 1N on NaCl-KCl mixtures. Given the high instrument force, it is likely the boron nitride supports a non-wetting contact angle, however, the design of the crucible was withheld from the article. Given this information, BN and graphite are the best-known candidates for KCl and MgCl<sub>2</sub> mixtures for sample container material with BN likely supporting a higher contact angle than graphite. Therefore, only boron nitride grades will be considered as viable materials moving forward.

### 3.1.4 Density Ratio

The first term of equation (5) on the right-hand-side represents the force due to the weight of the plunger. In this term is the ratio of the plunger density to the salt density assuming a cylindrical plunger shape. This ratio and the height of the plunger determine the magnitude of the weight force. This force can be greatly reduced by reducing the density of the material.

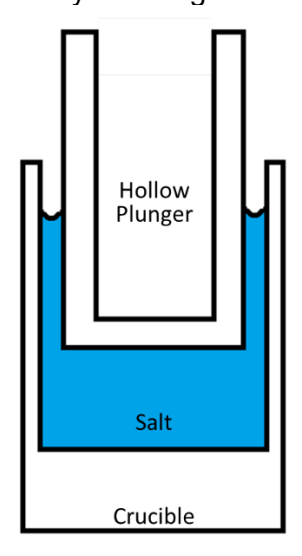


Figure 33. Cross-section of hollow plunger used to reduce density ratio.

The derivation assumes the plunger to be a cylindrical shape, but this is not exactly necessary. The plunger could be made of high-density BN on the salt facing side and have a hollowed out mid-section as seen in Figure 33. This would reduce the strength of the part and may have impacts on the effectiveness of the plunger if the plunger is imbalanced by the removal of material. However, the reduced density of the plunger could make higher density materials, such as noble metals, more viable.

Boron nitride is denser than the salt, and by using the hollow plunger design, BN could reduce the density of the plunger to be less dense than the salt. However, boron nitride is a ceramic with much lower material strength than metallic materials. The contact stress of handling, cleaning, and testing stresses necessarily increase the required wall thickness of the plunger. The necessity for a thick-walled hollow plunger may increase the manufacturing cost for a negligible change in plunger density. The decision was made to not include this feature for boron nitride material.

### 3.1.5 Material Strength and Cost

Boron nitride is a versatile material. It has three different crystal structures analogous to graphite, diamond, and wurtzite. Hexagonal boron nitride, like graphite, is soft and most stable at ambient conditions. The cubic boron nitride is extremely hard and comparable to diamond in structure. Hexagonal boron nitride (hBN) parts are typically pressed and sintered from a powder. These manufacturing processes use various pressures, temperatures, and additives to achieve a final product that is suitable for the application by varying the pore size, bulk density, material strength, conductivity, resistance to moisture, wettability, machinability, chemical compatibility, and thermal stability.

The oxygen content of hBN and molten salt heavily influences the contact angle and chemical compatibility of molten salt (Jenkins et al., 1968). Therefore, only hBN grades that have high purity and low oxygen content should be considered for use in this application. Precision Ceramics (a hBN parts manufacturer) has two, high-purity boron nitride grades, AX05 and PCBN1000 with published material strength properties, posted on the manufacturer's website. The material compositions are included in Table 6 and the strength properties are included in Table 7.

Grade	AX05	PCBN1000		
Oxygen	1	1		
Carbon	0.02	-		
Calcium	0.04	0.04		
Aluminum	-	0.01		
Silicon	-	0.01		
Other Impurities	0.05	-		
"-" Values not reported.				

Table 6. Maximum wt% concentrations of impurities in high-purity hBN grades.

The AX05 grade has a higher focus on reducing impurities. The open porosity of the AX05 grade is about 10% which allows a route for the liquid salt to penetrate the container material should the contact angle begin to wet the container material. The open porosity for the PCBN grade was not reported. Both materials have a similar oxygen impurity which will reduce the contact angle with the salt.

The AX05 has a considerably lower material strength which may lead to cracks and leaks under the repeated stress of handling and use. This property also lowers the machinability of the material and increases the part cost.

Of the two grades of hBN PCBN1000 is less expensive by a margin of about 12.5%.

Grade Unit AX05 PCBN1000 Density q/cm<sup>3</sup> 1.9 1.9 **Open Porosity** % 10 Compressive Strength MPa 25 | 40 II / 40 L Flexural Strength MPa 22 || / 21 ⊥ 13 || / 29 \( \tau Young's Modulus GPa 17 II / 71  $\perp$ Poisson's Ratio MPa 22 || / 21 \( \tau 14 || / 30 \( \pm "-" Values not reported.

Table 7. Material strength properties of high purity hBN grades.

### 3.1.6 Instrument Limits

This section designates the TMA system requirements on temperature, sample size, and sample container size.

The TMA instrument requires that the sample container diameter be less than 10 mm. The maximum temperature of the instrument is 1550°C with the current setup. The instrument supports atmosphere control and uses high purity argon as a cover gas.

Typical sample containers sold by the supplier have an outer bottom crucible diameter of about 6.5-6.8 mm, a sample reservoir volume of 300 mm<sup>3</sup>, and a length of about 9-15 mm. These crucibles are likely optimized to work well with the machine's capabilities and the crucible design for this experiment should not stray far from these dimensions.

### 3.2 Part Design

The two grades of hBN considered here are AX05 and PCBN1000. Since the contact angle of these materials is unknown, which significantly affects the stability of the measurement system, it was decided to include both materials in the crucible design. Once both materials have been tested, aspects of the design can be re-evaluated, such as whether the material allows salt to leak, absorbs salt, or if utilizing the more durable material is necessary.

The required wall thickness for the crucible was determined using the material strength properties of the AX05 material, as listed in Table 7, assuming the container would be subjected to pressures of approximately 1 MPa. Since the AX05 material has lower strength, one sample container was designed based on these properties and used for both materials, with AX05 serving as the limiting condition.

### 4.0 Conclusion

As a result of checking the bounding conditions of this application, we found boron nitride to be the material that best fits the KCl-MgCl<sub>2</sub> system. The high-purity grades AX05 and PCBN1000 provided by Precision Ceramics likely support a non-wetting contact angle, which is needed to prevent the liquid salt from leaking out of the crucible. A prototype TMA sample container was designed using the mechanical strength properties of the AX05 material. The dimensions of the sample container, especially the gap distance between the plunger and crucible, were determined using the physical model, equations (5) and (6).

## Pacific Northwest National Laboratory

902 Battelle Boulevard P.O. Box 999 Richland, WA 99354

1-888-375-PNNL (7665)

www.pnnl.gov